

DEEP CCD SURFACE PHOTOMETRY OF GALAXY CLUSTERS II: SEARCHING FOR  
INTRACLUSTER STARLIGHT IN NON-CD CLUSTERSJOHN J. FELDMEIER<sup>1,2</sup>, J. CHRISTOPHER MIHOS<sup>1,3,4</sup>, HEATHER L. MORRISON<sup>4</sup>, PAUL HARDING,  
NATHAN KAIB<sup>1,5</sup>  
johnf@bottom.astr.cwru.edu, hos@onager.astr.cwru.edu, heather@vegemite.astr.cwru.edu, harding@dropbear.astr.cwru.edu,  
kaib@astro.washington.edu

Department of Astronomy, Case Western Reserve University, 10900 Euclid Ave, Cleveland, OH 44106

AND

JOHN DUBINSKI  
dubinski@astro.utoronto.ca  
Department of Astronomy and Astrophysics, University of Toronto, 60 St. George St., Toronto, ON M5S  
3H8, Canada*Draft version October 31, 2018*

## ABSTRACT

We report the search for intracluster light in four Abell Type II/III (non-cD) galaxy clusters: Abell 801, 1234, 1553, & 1914. We find on average that these clusters contain  $\sim 10\%$  of their detected stellar luminosity in a diffuse component. We show that for two of the clusters the intracluster light closely follows the galaxy distribution, but in the other two cases, there are noticeable differences between the spatial distribution of the galaxies and the intracluster light. We report the results of a search for intracluster tidal debris in each cluster, and note that Abell 1914 in particular has a number of strong tidal features likely due to its status as a recent cluster merger. One of the Abell 1914 features appears to be spatially coincident with an extension seen in weak lensing maps, implying the feature traces a large amount of mass. We compare these results to numerical simulations of hierarchically-formed galaxy clusters, and find good general agreement between the observed and simulated images, although we also find that our observations sample only the brightest features of the intracluster light. Together, these results suggest that intracluster light can be a valuable tool in determining the evolutionary state of galaxy clusters.

*Subject headings:* galaxies: clusters: general — galaxies: clusters: individual (Abell 801, Abell 1234, Abell 1553, Abell 1914) — galaxies: interactions – galaxies: kinematics and dynamics

## 1. INTRODUCTION

As the most massive gravitationally bound structures in the universe, galaxy clusters stand to teach us much about the hierarchical assembly of matter in the universe. Clusters exhibit a wide variety of structural properties, from massive, X-ray luminous clusters dominated by early type galaxies (i.e., Coma) to irregular, spiral-rich clusters like the Ursa Major cluster, down to poor clusters and loose groups. The fact that many clusters are still obviously in the process of assembly can be seen via many tracers of substructure, such as X-ray isophotes, gravitational lensing maps, and kinematic and spatial substructure in the galaxy populations (see, e.g., reviews by Girardi & Biviano 2002 and Buote 2002)

A potentially powerful new tracer of the assembly history of clusters is intracluster light, the diffuse starlight which permeates many galaxy clusters. Once simply another curiosity of Zwicky (1951), individual intracluster stars have been clearly detected in several nearby galaxy clusters (Arnaboldi et al. 1996; Ferguson, Tanvir, & von Hippel 1998; Durrell et al. 2002; Feldmeier et al. 2004),

and through deep imaging this diffuse light has been detected in many more distant clusters (Uson, Boughn, & Kuhn 1991; Vilchez-Gómez, Pelló & Sanahuja 1994; Bernstein et al. 1995; Gonzalez et al. 2000). From the results to date, it is clear that intracluster light (ICL) is a common component of galaxy clusters and contains between 10% and 50% of the total stellar luminosity of the cluster, albeit with large uncertainties due to the intrinsic low surface brightness of the component (less than 1% of the night sky background).

The study of intracluster light is now entering a new phase, focusing on what can be learned about the evolution of galaxy clusters and their member galaxies using the ICL. Since galaxy clusters form hierarchically, and since the bulk of ICL production is believed to occur due to tidal-stripping from galaxy interactions and from the mean tidal field of the cluster (Richstone & Malumuth 1983; Miller 1983; Merritt 1984; Gnedin 2003), the properties of the ICL should be intimately tied to the dynamical evolution of clusters (e.g., Merritt 1984; Moore et al.

<sup>1</sup> Visiting Astronomer, Kitt Peak National Observatory, National Optical Astronomy Observatory, which is operated by the Association of Universities for Research in Astronomy, Inc. (AURA) under cooperative agreement with the National Science Foundation.

<sup>2</sup> NSF Astronomy and Astrophysics Postdoctoral Fellow

<sup>3</sup> Cottrell Scholar of Research Corporation and NSF CAREER fellow

<sup>4</sup> Also Department of Physics, Case Western Reserve University

<sup>5</sup> Current address: Astronomy Dept., Univ. of Washington, Box 351580, Seattle, WA 98195-1580

1996; Dubinski 1998; Mihos 2003; Napolitano et al. 2003; Willman et al. 2004). As clusters dynamically evolve, the fractional amount of ICL should increase if the cluster is isolated, and its spatial and dynamical structure should become well-mixed in the cluster potential well. As additional groups of galaxies enter the cluster, the fractional amount of ICL will briefly decrease, as the newer galaxies are initially unstripped, and then the fraction will increase as the additional galaxies suffer the effects of the cluster environment. The exact details of this overall evolution depend on the mass and accretion history of the cluster, tying the properties of the ICL directly to the cosmic history of cluster assembly.

The exact mechanisms of ICL production have implications for a number of other galaxy cluster studies. Ultra-compact dwarf galaxies (Drinkwater et al. 2003), the formation of S0 galaxies (Quilis, Moore, & Bower 2000, and references therein) and tidal debris in nearby clusters (Trentham & Mobasher 1998; Gregg & West 1998; Calcaneo-Roldan et al. 2000) may all be closely related to the ICL phenomenon. Since searches for individual intracluster stars in nearby galaxy clusters can be influenced by metallicity effects (Durrell et al. 2002; Feldmeier et al. 2004), knowing the dominant progenitor population is critical to avoid underestimating the true fraction of intracluster light. However, observational constraints on the ICL are still extremely poor, due largely to the scarcity of quantitative measurements of the ICL in clusters, especially over a range of cluster properties.

To address these questions, we have recently begun deep imaging of a sample of galaxy clusters to quantify the structure of ICL as a function of galaxy cluster properties (Feldmeier et al. 2002; hereafter Paper I). We have observed two cD-dominated (Bautz-Morgan Type I) galaxy clusters thus far (Abell 1413 and MKW 7); in each we quantify the extended cD envelope and find an excess of luminosity over a pure  $r^{1/4}$  law. However, this extended light is very smooth, and we find relatively little substructure in the ICL of either Abell 1413 or MKW 7. Again, however, both of these clusters are cD-dominated, and there are a number of reasons to expand our sample beyond cD-dominated galaxy clusters.

First, less than twenty percent of the total number of Abell clusters have a Bautz-Morgan type of I (Leir & van den Bergh 1977). Observations of ICL in Type I clusters may therefore not be representative of ICL structure in galaxy clusters as a whole. Second, the relation between intracluster light and cD envelopes is still unclear. Does the presence of a cD galaxy in a cluster always imply a large amount of intracluster starlight, or are ICL properties less correlated to the precise details of the cluster core? If intracluster stars are predominantly removed early in the cluster’s dynamical history (Merritt 1984), we would expect the properties of ICL to be intimately tied to the process of cD formation. If instead the bulk of the intracluster stars are removed from their parent galaxies by late tidal-stripping and related “galaxy harassment” scenarios operating on low luminosity galaxies (Richstone & Malumuth 1983; Moore et al. 1996), then the ICL properties may be less sensitive to the presence or absence of a cD galaxy in the cluster core. Finally, given the expected evolution of galaxy clusters under hierarchical structure

formation models (e.g., Merritt 1985; Dubinski 1998), it is expected that most rich galaxy clusters will eventually form cD galaxies, though the timescales involved could be quite long (up to thousands of Gyr; Adams & Laughlin 1999). Therefore Bautz-Morgan type II or III clusters may be less dynamically evolved proxies of the more evolved type I clusters, and ICL studies of these clusters may give us insight into the evolution of galaxy clusters at higher redshift and younger dynamical ages.

## 2. CLUSTER PROPERTIES

For this particular study, we focused on Abell clusters of Bautz-Morgan (Bautz & Morgan 1970) type of II, or greater, and similar richness (richness class 2). For our general survey goals and detailed selection criteria, see Paper I. Briefly, we focus on galaxy clusters that are smaller than the field of view of the telescope/detector combination (in this case, the KPNO 2m + TK2A chip; see §3), taking care to avoid nearby bright stars or galaxies that could be a significant source of scattered light. Table 1 gives the coordinates and basic information for each galaxy cluster observed in this study. Here, we briefly summarize the relevant properties for each cluster. In particular, we emphasize the known X-ray properties of our clusters, since X-ray detections are one of the most reliable indicators that a galaxy cluster is bona-fide, and X-ray observations give good indications of the mass and overall structure of a cluster.

Abell 801 has a Rood-Sastry type of B (b) (Struble & Rood 1987), a binary cluster where the central binary pair is connected with an optical bridge. It has been detected in X-rays multiple times (Soltan & Henry 1983; Böhringer et al. 2000), but has no measured X-ray temperature. Baum (1973) using photoelectric data, observed Abell 801 for intracluster light, and found that the intracluster light was  $\approx 16\%$  of the total cluster light, defined as the light outside of the  $\mu_V = 26$  isophote of the cluster galaxies. By extrapolating the luminosity function of Abell (1962), Baum claimed that approximately half of this excess could be attributed to dwarf galaxies below the Palomar Sky Survey plate limit, bringing the total amount of intracluster light to  $\approx 8\%$ . Gudehus (1989) claimed that the remaining excess light could be accounted for by the presence of dwarf galaxies below the surface brightness threshold, and the overlapping portions of bright galaxies, but gave no quantitative evidence to support this claim.

Abell 1234 has a Rood-Sastry type of L (line), where four or more of the ten brightest galaxies are arranged approximately collinearly with numerous fainter members located around them (Struble & Rood 1987). It has been detected in the X-ray (Burns et al. 1994; David, Forman, & Jones 1999) and significant X-ray substructure has been observed (Burns et al. 1994), but no X-ray temperature has been determined. Surface photometry of a radio galaxy in the core of this cluster has been obtained (Ledlow & Owen 1995), allowing us to compare our surface photometry on these spatial scales with others (§5.4). Finally, Struble & Rood (1987) note that this cluster is connected to Abell 1246.

Abell 1553 also has a Rood-Sastry type of L. From galaxy counts, Bucknell, Godwin, & Peach (1979) note that the entire cluster is considerably elongated, and Ya-

magata & Maehara (1986) claim that the cluster is quite large, with a cluster radius as large as  $R=11'.0$  (1.75 Mpc), though the measured core radius is much smaller  $R=2'.0$  (300 kpc). Struble & Rood (1987) note that this cluster appears closer than indicated for its distance class, implying possible foreground galaxy contamination. Abell 1553 has been detected in X-rays numerous times (e.g., Böhringer et al. 1994, 2000; Shibata et. al. 2001). White (2000) derived a temperature of  $4.18 \pm 0.15$  keV for Abell 1553 from ASCA data, but this temperature assumes a single thermal component model, and the temperature profile in the ASCA data is dropping significantly with radius, possibly due to poorer quality data or problems with background subtraction. The latter is more likely to be the case: Abell 1553 is directly behind the nearby Virgo cluster of galaxies. The center of Abell 1553 is  $\approx 1.8$  degrees to the south of M 87, and is clearly surrounded by X-ray emission from the foreground cluster (Böhringer et al. 1994; Shibata et. al. 2001). Virgo has an average X-ray temperature of  $\approx 2.5$  keV (Shibata et. al. 2001), therefore it is likely that Abell 1553's true temperature is larger than previously derived. The possible effect of Virgo's foreground light to our ICL observations will be discussed in §5.5

Finally, Abell 1914 also has a Rood-Sastry type of L. Its X-ray structure was claimed to be regular and smooth (Buote & Tsai 1996), but Jones et al. (2001) subsequently showed that X-ray images showed significant substructure in the core, that a conventional  $\beta$  model did not fit the data well, and that the cluster was in the process of merging. Abell 1914 has a high X-ray temperature ( $10.53^{+0.51}_{-0.50}$  keV; White 2000), although Ikebe et al. (2002) find a somewhat lower temperature of  $T = 8.41^{+0.60}_{-0.58}$  keV. Abell 1914 also has a measured Sunyaev-Zeldovich decrement (Grego et al. 2001; Jones et al. 2001), which with the high X-ray temperature, suggests that this cluster may be more massive than the other three in this study. Abell 1914 is one of approximately thirty galaxy clusters that are currently known to contain radio halos and relics (Giovannini, Tordi, & Feretti 1999; Kempner & Sarazin 2001), which are thought to be the result of cluster mergers (e.g., Feretti 1999; Buote 2001). Abell 1914 was analyzed using weak lensing by Dahle et al. (2002), who note that the light distribution and the weak lensing signal are highly elongated toward the south and west, supporting the merging state of this cluster. They also note the presence of several red and blue gravitational arc candidates around the brightest cluster galaxy.

### 3. OBSERVATIONS

The data for all four clusters were obtained over a seven night dark run in 2002 March 11–17, using the 2.1m telescope at Kitt Peak National Observatory<sup>6</sup>. The images were taken using a 2048 x 2048 Tektronix CCD (T2KA). With this setup, the field of view was  $10.4$  arcmin<sup>2</sup>, with each pixel imaging  $0.305''$  of sky. The gain was set at the default value of  $3.6$  e<sup>-</sup> ADU<sup>-1</sup> and the readout noise was  $4$  e<sup>-</sup> (1.1 ADU). All exposures were made through a

Washington  $M$  filter (see Paper I for a discussion on filter choice). We transformed these observations to Johnson  $V$  (§4.1), and unless otherwise stated, all surface brightnesses in this paper are given in  $V$  magnitudes. The first two nights of the run had photometric conditions, and excellent seeing ( $0''.8 - 1''.0$ ). On these nights, we observed Abell 1234 and Abell 1914. Unfortunately, before the third night, a front passed overhead, degrading the seeing to an average of  $2''.0$ , though conditions were still photometric for the next two nights. We observed Abell 801 and Abell 1553 under these degraded conditions.

An accurate flat-field is critical to the success of deep surface photometry such as ours. As mentioned in §1, we are interested in recovering a signal that is less than 1% of the sky background. Our flat field must be at least a few times more accurate than this 1% value for our data to be meaningful. For this reason, dome flat fields cannot be used due to possible scattered light, differing pupil illuminations, and intrinsic color differences. For similar reasons, twilight flats are also inadequate for our purposes. Therefore, dark sky flats are a necessity, and we obtained these flats in the manner described by Morrison et al. (1997). Half of the time was used observing the galaxy clusters, and the other half was used to obtain dark sky flats to guard against systematic errors due to telescope/detector flexure. The dark sky flat images were taken at pre-determined areas away from bright stars at approximately the same hour angle and declination as the cluster images (see Table 2). For each of the cluster and sky images, the exposure time was 900 s. We dithered the cluster images a few arcseconds between exposures to average out pixel-to-pixel flatfield variations, and we dithered the sky flat images by at least five arcminutes to avoid the overlapping wings of bright stars.

### 4. DATA REDUCTION

The data reduction procedures for this survey were given in detail in Paper I: we briefly summarize them here. Over-scan removal, bias subtraction and trimming of the images were done in the usual manner using IRAF<sup>7</sup>. Following the procedures of Paper I, we then corrected our data for the known non-linearity of the T2KA detector (Mochejska et al. 2001), using the following model:

$$I_e = I_i \cdot (c_1 + c_2 \cdot \frac{I_i}{32767} + c_3 \cdot (\frac{I_i}{32767})^2) \quad (1)$$

where  $I_i$  is the measured intensity, and  $I_e$  is the corrected intensity in ADU. The constants were determined by multiple linearity tests using dome flats taken during our run with a constant lamp voltage, but varying exposure time. We interleaved a series of one second exposures to track any change in the mean flux of the dome flat lamp. We found the following constants:

$$c_1 = 0.985 \pm 0.005, c_2 = -0.297 \pm 0.002, c_3 = 0.158 \pm 0.002 \quad (2)$$

Note that the  $c_1$  value is in good agreement with the results of Mochejska et al. (2001), but the other two values

<sup>6</sup> Kitt Peak National Observatory is a division of NOAO, which is operated by AURA, under cooperative agreement with the National Science Foundation.

<sup>7</sup> IRAF is distributed by the National Optical Astronomy Observatories, which are operated by the Association of Universities for Research in Astronomy, Inc., under cooperative agreement with the National Science Foundation.

are significantly larger in amplitude. This may be due to further changes with the T2KA detector over time. The actual correction to our surface brightness measurements will be extremely minor, because the intracluster light has a low flux (see Figure 3 of Paper I). Nevertheless, the uncertainty in our linearity correction is added to our final error model (see §6.4).

We next constructed a “master” sky flat from the 49 dark sky images taken. First, each individual sky flat was visually inspected to ensure that no bright stars or scattered light patterns were present in the image. In four of the images, we found a strong linear scattered light feature. We created a mask for each of the affected images to ignore these features, and a padding of  $\approx 30''$  surrounding them. No scattered light patterns were seen in any of the cluster images. Once the scattered light patterns were masked, the flat was then constructed using the iterative procedure described in detail in Morrison et al. (1997) and in Paper I. We correct for sky variations that are present in each image due to airglow (Roach & Gordon 1973; Wild 1997; Zheng et al. 1999) by fitting and dividing a normalized plane from each image. The entire process was iterated fifteen times, until the modes of each individual sky image were well determined.

The galaxy cluster images were then flat-fielded by this final flat, and were registered using stars common to all frames and the IRAF tasks GEOMAP and GEOTRANS, using a 2nd order polynomial fit. A preliminary sky value was found for each cluster image by finding the mode of two regions on each chip well away from the center of the cluster, and averaging the results. This sky value was then subtracted from each image. The median sky value for each cluster is given in Table 2, column 3, and correlates in the expected manner with lunar phase and time of night (Krisciunas & Schaefer 1991; Krisciunas 1997, and references therein). After applying the photometric zero point in (§4.1) below, these sky values range between  $\mu_V = 21.61$  and  $\mu_V = 21.12$ , in agreement with the expected influence of the moon. Since the source of sky brightness is mostly within the earth’s atmosphere, we removed our  $0.17 \text{ mag airmass}^{-1}$  extinction correction for our images around new moon, and found that the average brightness of the night sky at zenith near new moon was approximately  $\mu_V = 21.78$ . This is in good agreement with the measurements of Krisciunas (1997), who found a surface brightness of  $21.77 \pm 0.12$  at approximately the same time in the solar cycle (two years past the solar maximum).

With the overscan, bias-subtraction, flat-fielding and sky subtraction complete for each image, we then combined the images together, using a  $2\sigma$  clipped median as before, and scaling for airmass. We trimmed off portions of the combined image that were not in common between all of individual frames, which makes the final image for each cluster somewhat different in size (see Table 2 for final image sizes). The final images for each cluster are displayed in Figure 1.

#### 4.1. Photometric Zero Point:

The Landolt star fields SA 98, SA 107, SA 110, PG1633+099, Rubin 149, & Rubin 152 (Landolt 1992) were observed, giving us a total of 51 well-observed standard stars over a range of color and airmass. For the pur-

poses of our analysis, we converted our Washington  $M$  exposures to  $V$  band magnitudes during the photometric calibration process. A photometric zero point of  $\mu_V = 21.09 \pm 0.06$  (corresponding to  $1 \text{ ADU s}^{-1} \text{ pixel}^{-1}$ , and assuming a  $(B-V)$  color of 1.0) at unit airmass was determined. For a 900 s exposure this yields  $\mu_V = 28.48$  corresponding to  $1 \text{ ADU per pixel at unit airmass}$ , virtually identical to the zero point determined in Paper I. As our exposures were only taken in one filter, and we do not know the exact color of the intracluster light, we cannot add a color correction term to our target photometry, but from the standard star observations, we estimate its magnitude as less than 0.1 mag, over the entire likely color range of our target objects ( $0.8 \leq (B-V) \leq 1.3$ ). The color term is reasonably well fit as a linear function of  $(B-V)$ , with a slope of 0.2 magnitudes per magnitude of  $(B-V)$  color.

## 5. MASKING AND DETERMINATION OF ERRORS

We adopt approximate size distances to our galaxies in Table 2, column 7, assuming the redshifts given in Struble & Rood (1999), a Hubble constant,  $H_0 = 75 \text{ km s}^{-1} \text{ Mpc}^{-1}$ , and a cosmology of  $\Omega_m = 0.3$ ,  $\Omega_\Lambda = 0.7$ . At these small redshifts, these distances depend little on  $\Omega$ . Given these assumed distances, we give the angular scale of each of our cluster images in Table 2, column 8. The corresponding luminosity distance moduli, ignoring any K-corrections, are given in Table 2, column 9.

### 5.1. Masking

In order to reach the faintest possible surface brightness levels of the intracluster light, we must mask out all other sources — both stars and galaxies — in the frame. This allows us to be confident that we are measuring the true sky values of each image, and not compromising our data analysis with model-dependent assumptions from subtracting stars and galaxies. We mask the objects by creating a binary mask image for each cluster where good pixels are assigned a value of 1 and masked pixels a value of 0.

We first began by masking out the stars in each cluster image. Since we are concerned with a very low surface brightness signal, we determined the point spread function (PSF) out to very large radii. Using the DAOPHOT photometry package (Stetson 1987), we detected all of the stars in each cluster image down to a signal-to-noise of three, and used a subset of bright stars to determine the PSF in each cluster out to a radius of 20 pixels. We then used this preliminary PSF to mask out all of the stars and small galaxies around the brightest saturated star in each cluster image. Saturated stars have much higher signal-to-noise in the far wings on the PSF, which are our primary concern here. Other sources near the saturated star on each image, such as resolved galaxies and stellar diffraction spikes, were removed manually. Then the unmasked pixels from the each saturated star were averaged in radial annuli, and joined to the smaller-radius PSF (which measures the inner core of the star more accurately). We then compared the four independent PSFs, one from each cluster image, which are displayed in Figure 2.

Since the structure of PSF at large radii is due to effects such as atmospheric aerosols and microripples and dust on the telescope optics (Racine 1996; Beckers 1995), it should be relatively insensitive to the exact values of the

telescope seeing. This is confirmed in our data: the four independent profiles taken under varying seeing conditions agree quite well at intermediate radii. At still larger radii, the signal-to-noise of the profiles approach unity, and the profiles deviate from each other at a specific radius, which depends on the apparent magnitude of the saturated star. We therefore adopt the profile that extends securely to the largest radii, Abell 1234, and we join that large-scale surface brightness profile to the smaller scale profiles of the other clusters at a radius of 12.2 arcseconds. Using these large-radius PSFs, and the list of stars found by DAOPHOT, we masked all stellar sources in each cluster image out to a radius where the magnitude-scaled PSF was 1 ADU above the sky value.

Next, we masked out all of the galaxies in each cluster. Since unresolved galaxies would have already been treated as point sources, and thus been masked by the DAOPHOT procedure above, but many resolved sources remain in each cluster. As in Paper I, we masked these sources using the segmentation image from the SExtractor software package (V2.2.2; Bertin & Arnouts 1996), using identical parameters and the correction algorithms we used in Paper I to improve the masking. Finally, the images multiplied by the mask were visually inspected, and any regions that needed further masking were masked using IMEDIT. These manual corrections were usually due to “islands” of unmasked pixels (which have sizes of a few pixels and are discussed in detail in Paper I), and were typically less than 0.3% of the total image area.

## 5.2. Final Sky Subtraction, and Large-scale Flat-Fielding Errors

Accurate sky subtraction is crucial to determine the true amount of intracluster starlight in each cluster, and is one of the dominant sources of error in our analysis. We found a more accurate sky level for each cluster by using the masked image. We first binned up each cluster image into bins of  $49 \times 49$  pixels. For each bin, we calculated a robust average (Morrison, Boroson, & Harding 1994), ignoring all masked pixels. We then fit and subtract a plane from each masked, binned cluster image, using the IMSURFIT task in IRAF, taking care to use regions on each image that are well away from the cluster core. We determined the locations of these regions by first excluding any pixel within two arcminutes of radius of the cluster core ( $\approx 340$  kpc). Then, we examined the binned image visually to find regions that were relatively free of any suspected ICL and bright stars and galaxies, to avoid any low-surface brightness emission that remained unmasked. The average radii for these sky subtraction regions are typically 1 Mpc. The mean corrections from this plane subtraction are small: less than 1.0 ADU for the clusters on average. However, we emphasize that this process will remove any smooth ICL that covers the entire image. We then re-create the histogram of sky values in  $49 \times 49$  pixel bins well away from the center of each cluster. We also require that the bins contain at least 100 unmasked pixels to be included in this revised histogram. These histograms are displayed in Figure 3. The width of the histograms provides a measure of our uncertainties due to large-scale flat-fielding errors and the faint outer wings of stars and galaxies that remain unmasked, even after the involved procedure above.

For Abell 801 and Abell 1234, the sky histograms are well-defined, with a single mode, and relatively narrow distribution. We adopted the standard deviation in the sky histogram as the large-scale flat-fielding error in these two cases. We note that the values derived ( $\approx 0.6$  ADU) are noticeably smaller than the values derived for our first two galaxy clusters in Paper I ( $\approx 1.0$  ADU), which we attribute to the larger number of sky flats available for this data set (49 vs 20). However, for Abell 1553 and Abell 1914, the sky histograms are clearly of lesser quality. There is a clear bi-modality present in both histograms, and the width of the histograms is much larger than the other two clusters. It is important to note that the histogram range displayed in both of these clusters is  $\pm 3$  ADU from the sky level, which corresponds to a surface brightness of  $\mu_V = 27.2$ , or 6.0 magnitudes below the sky level. Nevertheless, the effect is a systematic error of the data, and cannot be ignored. The sky histograms show a clear pattern along the y-axis of the image, corresponding to an E-W direction on the sky. Figure 4 shows this systematic effect for both Abell 1553 and Abell 1914 sky bins.

Since all four clusters were flat-fielded with the same sky flat (§4), this effect must be due to some systematic difference between the two groups of clusters (801 and 1234 versus 1553 and 1914). There are no clear differences between the two groups in seeing, lunar phase, or time of night observed. However, we do note that the hour angle that the clusters were observed is slightly different between the two groups. In Table 2, column 5, we give the mean hour angle of the observations of each cluster. Abell 801 and 1234 tended to be observed east of zenith, while Abell 1553 and 1914 were observed slightly west of zenith. The sky frames also have an average hour angle that is slightly east of the zenith. Therefore, we attribute the large-scale flat-fielding error to flexure in the telescope and detector as it tracks across the sky, and small mismatches between the hour angle of our observations and the sky frames. These small mismatches would cause a slightly different vignetting pattern, and hence a different flat field image.

If the large-scale flat-fielding error is indeed due to the telescope’s hour angle, we could in principle partially correct this effect to by creating two sky flats, one for the eastern portion of our data and another for the western. However, the number of sky flat images on either side of zenith are unequal, and we would therefore create a noisier flat for one half of our data. In effect, this approach would have us simply trading one source of flat-fielding error for another in our analysis. The large-scale flat-fielding error could also be corrected by fitting a function to the sky bins shown in Figure 4, and dividing the data by this function. However, this approach introduces a new source of uncertainty from the functional fit to this higher-order structure in the flat field. This is particularly worrisome since our clusters are always centered on the images, and may bias the fit in such a way to artificially produce (or suppress) features which mimic the large-scale ICL we are trying to detect. We therefore chose the most conservative approach – to not attempt any higher-order corrections to the flat field – and adopt a large value for the large-scale flat-fielding error for Abell 1553 and 1914 based on a visual inspection of the uncorrected sky histograms. Although this limits the surface brightness depths we reach in these

clusters, we believe this solution to be one which is least likely to bias our quantitative measurement of the ICL in these clusters. The adopted large-scale flat-fielding errors for all of the clusters is given in Table 3, columns 1–4, where we note that even in the worst case the flat-fielding error is smaller than 0.35%.

### 5.3. Limits to Our Precision

The flux error model is described in detail in the Appendix, and is used in all of our analysis. At low surface brightnesses, the dominant source of error are large-scale flat-fielding and sky subtraction errors, which are systematic, and do not depend on the number of pixels averaged. Using our error model applied to the sky bins, we determined the error limit for each cluster image in ADU, which we present in Table 3, column 5. This limiting uncertainty for each cluster can be converted into a surface brightness limit. Many authors prefer to quote the  $1\sigma$  limit as their observational limit, and we give that limit,  $\mu_{1\sigma}$ , for our cluster observations in Table 3, column 6. These values range between  $\mu_V=28$  and 29. However, in order to be conservative, we will sometimes use a signal-to-noise ratio of five in our analysis. That limit,  $\mu_{5\sigma}$ , is given in Table 3, column 7, and range between  $\mu_V=26$  and 27, respectively. As an independent check of our error model, we compared the expected standard deviation of the sky background from the error model against the average standard deviation of the sky in each cluster image found by SExtractor. We found that our error model actually overestimated the measured standard deviation by 10–20%: we attribute to this to the large-scale flat-fielding fluctuations seen in the data, but treated as sky variations in the SExtractor determination. We are confident that our flux error model is a good description of the data.

### 5.4. Comparison to previous results

As a consistency check, we compare our surface photometry to other published results from our clusters. Unfortunately for the clusters in this study, the only galaxy that has published surface photometry results is 1119+216 (A1234-A;  $\alpha = 11\text{h } 22\text{m } 29.95\text{s}$ ,  $\delta = +21^\circ 24' 21''$ , J2000.0), a radio galaxy studied by Ledlow & Owen (1995; see Owen, White & Ge 1993 for a finding chart). The surface photometry of Ledlow & Owen (1995) was taken through a Cousins ( $R_C$ ) scale, so we adopt the identical color transformation given by these authors ( $V-R_C = 0.59$ ) for comparison purposes.

We determine the surface brightness profile of 1119+216 using the ELLIPSE task in IRAF/STSDAS (Busko 1996), based on the algorithms of Jedrzejewski (1987). We cannot compare the surface brightness profiles in detail, since they are not published in Ledlow & Owen (1995). Instead we compare our ELLIPSE results against theirs at  $r_{24.5}$ , where the  $R_C$  surface brightness reaches  $24.5\text{ mag arcsec}^{-2}$ . The comparison is shown in Table 4. The distances are computed assuming a  $H_0 = 75\text{ km s}^{-1}\text{ Mpc}^{-1}$ ,  $q_0 = 0$  cosmology, to stay consistent with Ledlow & Owen (1995).

There is good agreement between the parameters derived from both datasets. In the case of the position angle derived, we find from our data that at the radius corresponding to  $r_{24.5}$  is located within a 10 degree elliptical isophote twist, making it difficult to measure the position

angle precisely. We conclude that within the errors, our surface photometry for Abell 1234 is in agreement with previously published work, though our observations reach to a much fainter surface brightness.

### 5.5. Abell 1553 and Virgo’s ICL

As we have previously noted, Abell 1553 lies behind the the Virgo cluster, which is known to have intracluster light of its own (Arnaboldi et al. 1996; Feldmeier, Ciardullo, & Jacoby 1998; Ferguson, Tanvir, & von Hippel 1998; Durrell et al. 2002). Does the presence of this foreground intracluster light affect our measurements of the ICL of Abell 1553? Conversely, can we learn anything about the foreground Virgo ICL from our observations of Abell 1553?

Since we fit and subtract a plane from each individual cluster image before averaging the images together, any smooth ICL from the Virgo cluster in our Abell 1553 frames will have been removed along with the sky emission. Due to the large fluctuations (10–30%) in the modal sky value due to atmospheric effects such as airglow, it is almost impossible that we can directly detect any constant excess emission that we can attribute to Virgo’s ICL.

However, we can set an interesting limit on the amount of intracluster light in the region in front of Abell 1553. Virgo’s ICL is close enough that any emission from it should also have surface brightness fluctuations. Tonry & Schneider (1988) originally showed that the variance (in ADU) of the mean surface brightness of a stellar population due to luminosity fluctuations (their eq. 10) is:

$$\sigma_L^2 = \bar{g}(x, y)t(10\text{pc}/d)^2 10^{-0.4(\bar{M}-m_1)} \quad (3)$$

where  $\bar{g}(x, y)$  is the mean sky-subtracted signal from the source,  $t$  is the exposure time of a single observation,  $d$  is the distance to the stellar population,  $\bar{M}$  is the mean, luminosity-weighted absolute magnitude of a stellar population and  $m_1$  is the magnitude of 1 ADU  $\text{s}^{-1}\text{ pixel}^{-1}$ . Normally, this equation is used to find  $d$ , given a measurement of  $\sigma_L^2$ , and  $\bar{g}(x, y)$ . Here, our goal will be to place a firm upper limit on  $\bar{g}(x, y)$ , assuming a distance to the Virgo cluster, and a measurement of  $\sigma_L$ .

To obtain a firm upper limit to  $\sigma_L$  on a large spatial scale, we proceed in the following manner. Since our error model already fully describes the data (§5.3), to take a reasonable limit, we assume that the intrinsic surface brightness fluctuations have been inadvertently folded into the large-scale flat-fielding error. To separate the two effects, we take the measurements of Abell 1553’s large-scale flat-fielding error presented in Figure 4, and fit and subtract a quadratic function through a least squares fit. After subtracting the quadratic, we find the standard deviation of the points using a  $3\sigma$  clip of 0.670 ADU. This is only slightly higher than the minimum large-scale flat fielding error we derived for Abell 801 (0.6 ADU). When we remove the minimum flat-fielding error expected in quadrature, we are left with a value for  $\sigma_L = 0.297$  ADU. We next need to apply a correction for the effects of seeing, which artificially suppresses the intrinsic surface brightness fluctuations. We obtain this correction factor by taking a simulated image with mean zero and known  $\sigma_L$ , and convolving it with the measured PSF (§5.1). The PSF-convolved image had a measured  $\sigma_L$  which was a factor of 1.67 lower than the true value; we apply this correction

factor to our measurement of Abell 1553 to get a final value of  $\sigma_L = 0.497$  ADU. Since this represents the maximum value possible for the intrinsic SBF of the Virgo ICL, it is clear that there will be little or no effect on our studies of the ICL in Abell 1553 itself on large spatial scales.

Using the relationship between SBF and surface brightness, we can now place limits on the surface brightness of the Virgo ICL from our data. After assuming a distance to Virgo of 15 Mpc, the photometric zero point  $m_1 = 21.092$ , and a  $\overline{M_V}$  value of 1, characteristic of old stellar populations (Tonry, Ajhar, & Luppino 1990), we find that our upper limit value for  $\overline{g}(x, y)$  is 5.7 ADU, corresponding to a surface brightness of  $\mu_V = 26.6$ . This surface brightness limit is in rough agreement with values derived from direct observations of Virgo’s intracluster stars ( $\mu_V \approx 27\text{--}29$ ; Durrell et al. 2002; Feldmeier et al. 2004), but is not faint enough to constrain the amount of Virgo ICL significantly. Nonetheless, in the future, surface brightness fluctuations may provide an important independent constraint on the ICL in nearby clusters.

## 6. MEASURING THE INTRACLUSTER LIGHT

The total cluster starlight in the galaxy clusters studied in Paper I was clearly dominated by the central cD galaxy and the intracluster light. This made analysis reasonably straightforward: we masked the other galaxies of the cluster, and treated the cD galaxy and the ICL as a single, elliptically symmetric, luminous component. However, in the clusters studied here, the situation is more complicated. There is no central cD galaxy dominating the cluster, and the intracluster light may not be elliptically symmetric (or even present). With the bulk of the cluster’s optical light split evenly between several galaxies, it becomes even more difficult to separate the galaxy light from the intracluster light in a clear, model-independent fashion. Therefore, we have chosen to analyze these clusters in several different ways in an effort to place reasonable limits on the amount and spatial distribution of ICL in each cluster. We unmask the light coming from galaxies, leaving only the point sources masked in each galaxy cluster.

### 6.1. Isophotal Measurements

We first separated the optical light from galaxies and the ICL using the simplest method possible: through an isophotal cutoff. The choice of a unique isophotal cutoff is somewhat problematic, however. Galaxies are often characterized by relatively high surface brightness, and a common definition of the size of a galaxy is  $R_{25}$ , the radius at which the surface brightness drops to  $\mu_B = 25$  (de Vaucouleurs et al. 1991). In reality, however, this tends to underestimate the sizes of galaxies, which often extend to or exist at much lower surface brightnesses (i.e., Morrison, Boroson, & Harding 1994; Bothun, Impy, & McGaugh 1997; Fry et al. 1999). Another benchmark of the surface brightness at which we might start to define the intracluster light is to look at the surface brightness of tidal debris in nearby interacting systems. For example, the merging system NGC 7252 has two tidal tails with surface brightnesses  $\mu_V \sim 26\text{--}27$  (Hibbard et al. 1994, assuming B-V  $\sim 1$ ). As there is no clear expectation that any single surface brightness limit can distinguish galaxies from intracluster

light, we explore a range of thresholds ( $\mu_{limit} = 26\text{--}27.5$ ) for characterizing the diffuse light in clusters.

For this exercise we first identified all stellar sources on each cluster image, and masked them out using our large-scale PSF. We defined a stellar source as all objects from our earlier SExtractor catalogs that had a star/galaxy classifier value greater than 0.8. We then masked each individual pixel that had a corresponding surface brightness brighter than some limit  $\mu_{limit}$ . We used four surface brightness limits, to bracket the respective depths of our cluster images ( $\mu_{limit} = 26, 26.5, 27, \text{ and } 27.5$ ). In order to avoid biasing our results to negative flux, we also masked the corresponding negative pixels to the identical negative ADU value as the positive surface brightness limit. This ensured that the mean flux of an empty region of sky approached zero as the isophotal limit was reduced. An image of the core of Abell 1234 masked in this manner is shown in Figure 5.

To determine the relative fraction of the ICL light compared to the galaxy light, we then created an inverse mask to isolate and measure galaxy light – in this inverse mask, point sources and all pixels fainter than  $\mu_{limit}$  were masked instead. We then summed the un-masked pixels in each mask, and determined the flux ratio for the cluster region, after correcting for the area lost to the ICL from the cluster galaxies. The errors in the flux ratio were determined by our flux error model, and are completely dominated by the large-scale flat-fielding errors. We note that this method gives us a luminosity-weighted average ratio over the entire cluster, and washes away any radial structure in the ICL.

Table 5 gives the fractional flux in the ICL for each value of  $\mu_{limit}$ . We show the results for Table 5 graphically in Figure 6. The corresponding luminosities and luminosity densities are given in Table 6. We find that the fraction of ICL measured in this way varies from 28% to 5% when we restrict our measurements to above  $\mu_{5\sigma}$ . Our measurement of Abell 801 at  $\mu_{limit} = 26.0$  is  $16 \pm 4.7\%$ , in remarkable agreement with early measurements by Baum (1973), who found a fraction of 16% at the same isophotal cutoff using photoelectric photometry with single-channel scanning of the entire cluster. The ICL luminosities of each cluster vary from  $1 \times 10^{11} L_\odot$  to  $0.3 \times 10^{11} L_\odot$ , roughly equal to that of a few Milky Way galaxies. The luminosity densities found are roughly equivalent to those found from intracluster star studies seen from nearby clusters (Durrell et al. 2002; Feldmeier et al. 2004).

There are a number of additional uncertainties to these results that are difficult to quantify precisely. First, since we masked all unresolved sources in the cluster images, we might exclude unresolved galaxies in each cluster. This would tend to artificially increase our measurement of the ICL fraction. However, at the same time, we have included all non-stellar objects in the frame as “cluster” galaxies. Since there are a number of foreground and background galaxies in each cluster frame, including them would tend to decrease the fractional ICL flux determined.

From inspection of our non-stellar luminosity functions from the SExtractor catalogs, our observations reach at least five magnitudes below  $M^*$  (Schechter 1976) for these clusters, making any unresolved galaxies a small portion of the total cluster luminosity. If we assume that the lumi-

osity function of our clusters are similar to that measured in Virgo by Trentham & Hodgkin (2002), we find that at most 2% of the cluster luminosity can be lost in this way. Similarly, from spectroscopic observations of cluster galaxies at similar redshifts, Wilson et al. (1997) estimate the contamination rate for bright galaxies to be no higher than 25% over the entire cluster, and is likely to be significantly smaller in the cluster core.

However, the largest significant uncertainty is likely to be the choice of isophotal cutoff for the measurement. Galaxies are not all truncated at a fixed surface brightness limit, and an examination of Figure 5 clearly shows what appears to be galaxy light “leaking” around the edges of the isophotal masks for brighter galaxies. To estimate the magnitude of this effect, we quantify for a fiducial elliptical galaxy the fractional luminosity located outside the different isophotal cutoffs we adopt. Since most galaxies in the cluster cores are early-type, this should give us a first-order approximation to the amount of light we could be misidentifying as ICL. We use the extremely well-studied galaxy NGC 3379, which has been found to follow a de Vaucouleurs (1948) profile over ten magnitudes of surface brightness. We take the surface photometry of Capaccioli et al. (1990), assuming a (B–V) color of 0.96 (de Vaucouleurs et al. 1991), and applying the best fit  $r^{1/4}$  model, we determine the fraction of galaxy light outside of each isophote. This fraction is given in the row entitled “NGC 3379” in Table 5.

We find that up to 8% of the total measured ICL could be attributed to the extended nature of galaxies. However, this is likely to be a firm upper limit, and is strongly dependent on the exact radial extent of galaxies in clusters. Since galaxies in clusters are truncated by the mean tidal field of the cluster (i.e., Merritt 1984; Gnedin 2003), it is likely that the amount of galaxy light outside a particular  $\mu_{limit}$  is less than calculated for the galaxy NGC 3379. NGC 3379 is contained within the Leo I galaxy group, making it unlikely that it has been severely tidally truncated. Since the actual tidal radius for each galaxy depends sensitively on the velocity dispersion of the cluster and the velocity dispersion and orbital properties of the galaxy, we adopt a small radius to place a limit on this effect. We take the results of Merritt (1984), which give the smallest tidal radii of around  $\sim 20$  kpc. If we artificially truncate the NGC 3379 results to this radius, which corresponds to a surface brightness of  $\mu_V = 26.5$ , we obtain the results of the row entitled “NGC 3379 (trunc)” in Table 5. In this case, the extended galaxy light contributes substantially less to the measurement of the fractional ICL flux.

Given the large uncertainty in the above effects, we conclude that the average fraction of ICL in these clusters is approximately 10%, and certainly no more than 20% of the light seen in galaxies. This is consistent with studies of intracluster light in nearby clusters (Arnaboldi et al. 1996; Feldmeier, Ciardullo, & Jacoby 1998; Ferguson, Tanvir, & von Hippel 1998; Durrell et al. 2002; Feldmeier et al. 2004) but is less than the measured amount for the Coma Cluster (50%; Bernstein et al. 1995), and less than found for clusters with large cD galaxies ( $\sim 20$ –40%; Paper I; Schombert 1988).

## 6.2. The Spatial Distribution of the ICL

To understand the basic properties of the spatial distribution of the ICL in these clusters, we began by visually examining the data. Using the identical binning procedure used above, we binned each cluster image into small bins, including the galaxy light, but excluding all identified point sources. By experimentation, we found that a bin size of  $11 \times 11$  pixels was the best compromise between spatial resolution and signal-to-noise for this purpose. These images are plotted in Figure 7. In order to highlight structure at different surface brightness levels, we have color-coded the images by surface brightness: black shows bins with surface brightnesses from  $\mu_V = 20$  to 24, red shows  $\mu_V = 24$  to 26, green shows  $\mu_V = 26$  to 27, and blue shows  $\mu_V = 26$  to 27. Masked bins, or bins with surface brightnesses below  $\mu_V = 28$ , are left uncolored. For Abell 1553 and Abell 1914, where the large-scale flat fielding errors are significantly larger, we do not color the  $\mu_V = 27$  to 28 bins. By adopting these limits, we ensure that all bins that are colored in Figure 7 are at least  $2\sigma$  above the sky background.

There is a striking difference between the clusters in the spatial distribution of their ICL. In the case of Abell 801 and Abell 1553, the ICL appears to closely follow the galaxy light, and in Abell 801 at least, appears to have elliptical symmetry. Generally, the differing isophotal levels have similar geometric structure in these clusters. In contrast, Abell 1234 and Abell 1914 show a very different behavior. In these clusters, the ICL follows the galaxy light less well, and there are asymmetric features that are clearly visible in the images. The size of these features are large, on order of a few arcminutes, corresponding to a linear size of a few hundred kpc. In these clusters, the different isophotal levels have markedly different morphologies.

To confirm and quantify these qualitative results, we determined the median spatial centroid of the bins in each cluster at differing surface brightness limits corresponding to the levels shown in Figure 7. We note that this centroid is an unweighted median of the bin positions at each isophotal level, and is not a luminosity-weighted median. To avoid contamination from background sources, we limited the centroid determination to the regions used in measuring the total ICL in §6.1. We determined the errors in our centroids by bootstrap resampling the data 50,000 times, and measuring the standard deviation of these determinations. We found that in every case, the error of the median centroid was half of a bin size or less. We also tested the median centroid on an artificial star constructed from our large-scale PSF (§5.1), and found that the centroid moved less than a few pixels, over the range of surface brightness of interest. Since the values for the median are by construction quantized on a  $11 \times 11$  pixel grid, we took a conservative value for the error of the centroid as 11 pixels ( $3.3''$ ). The positions for each of the centroids are given in Figure 8.

We found that for both Abell 1234 and Abell 1914, there were significant ( $4\sigma$  and  $6\sigma$ , respectively) displacements of the centroid in both the north-south and east-west directions from the high surface brightness centroids to the lower surface brightness ones. Specifically, Abell 1234’s measured centroid moved  $\approx 16''$  to the southeast when the surface brightness limit was extended from  $\mu_V = 24$  to



$\mu_V = 28$ . This shift can be clearly be seen as due to a low surface brightness feature (colored in blue in Figure 7) that is approximately perpendicular to the main cluster axis (colored in red and green bins), and is displaced to the east. Abell 1914’s centroid moved  $\approx 28''$  northeast as the surface brightness limit was increased to  $\mu_V = 26$ , and then moved  $\approx 20''$  southwest, as the surface brightness limits were increased to  $\mu_V = 27$ . These shifts can be attributed to the large envelope of light surrounding the cluster galaxies that is clearly offset from the galaxy distribution. By contrast, Abell 801 and Abell 1234’s centroids remained within  $2\sigma$  of the original determination at all surface brightness levels. There appears to be no visible pattern to the offsets derived to these clusters that correspond with other surface brightness features.

In conclusion, we find a range of properties for the spatial distribution of the intracluster light. Clearly, in some cases, the cluster light closely follows the galaxies, but in other cases, there are noticeable changes in both the centroid and the shape of the luminosity distribution.

### 6.3. The Search For Tidal Features

With the global properties of intracluster light established for each cluster, we now search for any large-scale tidal debris. We emphasize that we are focusing on debris that is of significant size compared to the extent of each cluster. In all of the clusters, we find many morphologically unusual small sources, but without color or redshift information we cannot be confident that these sources belong to the cluster, and are not foreground or background objects. We therefore leave their study for the future.

For the purposes of this discussion, we define a tidal debris arc as an extremely elongated (ellipticity  $\geq 0.5$ ) discrete object that can be detected visually, and a tidal plume as any broader diffuse emission not fixed to any single galaxy. Two of us (J.F., C.M.), searched each cluster image independently, and noted any features from a visual inspection that were detected in common. We note that searching for arc-like features will be strongly dependent on the seeing, and so we expect fewer features detected in Abell 801 and Abell 1553 than in the other clusters. However, larger plume-shaped features should still be visible in all clusters, since their spatial scale is much larger than the seeing disk.

In both Abell 801 and Abell 1234, we found no large-scale discrete tidal features that could be attributed to the intracluster light. We did detect a few smaller features around the central elliptical galaxies in Abell 801 that resemble the low surface brightness “shells” seen by Malin & Carter (1983), but due to the poor seeing more study will be needed to confirm these objects. In Abell 1234 we find a number of small-scale diffuse objects, but none of these can clearly be attributed to tidal features or gravitational lensing based on our imaging alone. In both Abell 801 and Abell 1234, we do find that the galaxies in general appear to be surrounded by a common envelope of diffuse intracluster light.

In contrast, Abell 1553 has a bright plume-like feature extending from the southeast of one of the central galaxies, which is plotted in Figure 9. It can also be clearly seen in Figure 7 as the green region just above the masked star in the center of the image. From inspection of the origi-

nal image (Figure 9, left), there is a roughly semi-circular plume (hereafter referred to as the bright plume) that is  $\approx 13''$  in radius, and has a mean surface brightness of  $\mu_V \approx 25$ . After inspection of the binned-up data, we also found a fainter plume-like object (hereafter referred to as the faint plume) that is along the path of the bright plume, but had a wider opening angle, and a much fainter mean surface brightness ( $\mu_V \approx 26.2$ ). We plot this fainter plume in the right panel of Figure 9, where we denote the area of the plume as the spatial bins with white central pixels. There is an abrupt change in surface brightness marking the transition between these two features, making it difficult to determine whether they comprise a single object, or are distinct structures. We measured the apparent magnitudes of both plumes, and found a total magnitude of  $m_v \sim 19.0$  for the bright plume and  $m_v \sim 18.8$  for the faint plumes, corresponding to an absolute magnitude of  $V \sim -20.3$  and  $-20.5$ . These are each approximately a Milky Way’s worth of luminosity, spread out over an areas of approximately  $2000 \text{ kpc}^2$  and  $5000 \text{ kpc}^2$ , respectively. Curiously, at the location of the faint plume the distribution of cluster galaxies appears to turn abruptly, from running northwest to southeast, to extending due east. It is unclear whether this is a coincidence or has some relation to the tidal plume structure.

In Abell 1914, there is a wealth of diffuse structure that is immediately apparent to the eye. We detect five large-scale features: two arc-like features, one to the west of the cluster core, and one in the geometric center of the cluster, and three tidal plumes each leading from the triangle formed from the brightest galaxies in the cluster, which we denote as the northwest plume, the southwest plume, and the eastern plume, respectively. They are all displayed in Figure 10, and are discussed in detail below.

The western arc is displayed in Figure 11. The arc is approximately  $1'$  long ( $\approx 160 \text{ kpc}$ ), and has a maximum width of  $12''$  ( $\approx 30 \text{ kpc}$ ), though in portions the arc becomes as narrow as  $2.2''$  ( $\approx 6 \text{ kpc}$ ). The arc appears to have a bulge or bifurcation approximately halfway along its length. The maximum surface brightness of the arc is  $\mu_V \approx 25.4$ , and the median surface brightness is  $\mu_V \approx 26.1$ . The properties of this arc candidate in physical size and in surface brightness are very similar to the tidal debris arcs seen in the nearby Coma and Centaurus clusters (Trentham & Mobasher 1998; Gregg & West 1998; Calcaño-Roldán, et al. 2000, ; see Paper I, Table 5 for a summary). Although Dahle et al. (2002) note the presence of several gravitational arc candidates in their images of Abell 1914, we believe that it is unlikely that this particular arc is due to gravitational lensing. Specifically, the arc is radially resolved, widens significantly along its path, and is not tangential to the mass distribution. The cause of the bulge or bifurcation midway through the arc candidate is unknown: it may be due to a gravitational disturbance from a passing galaxy.

The central arc is  $5.4''$  long and  $1.7''$  wide. It is visually unremarkable, and appears almost rectangular. It has a larger mean surface brightness  $\mu_V \approx 25$ , and a peak surface brightness of  $\mu_V \approx 24.6$ . This arc may well be due to gravitational lensing: it is short, tangential to a portion of the mass distribution, and is radially narrower than the western arc. It appears to lie within a common envelope

of the nearby galaxies.

The southwest plume is extremely large, more akin to an extended envelope, and can be seen most clearly in Figure 7 as the extremely large asymmetry colored in green to the upper right of the cluster center. This structure lies along one of the cluster axes, and a complex of several luminous galaxies lies within it. It has an enormous extent, at least  $98''$  along the axis of the cluster and  $112''$  wide, corresponding to an approximate physical size of 270 by 300 kpc. It has a mean surface brightness of  $\mu_V \approx 26.7$ . However, due to its spatial proximity to the edge of the large-scale flat fielding pattern, its irregular structure, and its low surface brightness, we do not attempt to determine a total magnitude for this feature, though it should be quite large.

The northwest plume can be seen as a narrow, roughly triangular plume extending away from one of the central elliptical galaxies. It has a mean surface brightness of  $\mu_V \approx 26$ , and has a width of  $\approx 11''$ , and a height of  $\approx 22''$ , corresponding to physical dimensions of  $\approx 30$  and 60 kpc, respectively. The total magnitude of this feature is  $m_v \approx 20.7$ , corresponding to an absolute magnitude comparable to a small spiral galaxy.

Of all the tidal features seen however, the most striking is the large plume to the east of the cluster core, which is displayed in Figure 12. The plume is located at the end of a linear structure of six luminous elliptical/S0 galaxies that show signs of tidal interaction, and lie within a common surface brightness envelope. The eastern plume has a size of  $52''$  in the east-west direction, and  $39''$  in the north-south direction. The mean surface brightness of this feature is  $\mu_V \approx 26.4$ . The total magnitude from this plume is enormous,  $V \sim -21.3$ , comparable to the entire optical luminosity of M31. The plume appears sharp-edged – the surface brightness drops by over a factor of two (down to the background level) over  $3.4''$  (9 kpc) at the southern edge. Such a sharp edge strongly implies a recent tidal origin for this feature, since if it had been torn out early in the cluster’s history, or in the outskirts of the cluster, any sharp features would be dynamically heated and mixed away by the tidal field of the cluster and its member galaxies.

The most remarkable feature of this plume, however, is that it lies on top of a feature seen through gravitational lensing. Specifically, the eastern plume can be clearly seen in the weak lensing map of Dahle et al. (2002), a property not seen for the other plumes in Abell 1914. This implies that a large fraction of matter in addition to the optically luminous matter must be associated with this particular plume, since the intracluster light is a minuscule part of the cluster’s total mass.

Because this plume does appear to trace mass as inferred from the lensing maps, we might also expect to observe it in X-ray emission. We have compared an 8.7ks *ROSAT* PSPC archival image (PI: Böhringer) of Abell 1914 to our optical image, binned to the same spatial resolution (15 arcseconds) as the PSPC image. We find, as Jones et al. (2001) did, that the X-ray emission from Abell 1914 shows significant substructure in the core and there appears to be a small extension in flux to the east, which might correspond to the linear structure of the six elliptical/S0 galaxies mentioned above. While we see no significant emis-

sion associated with the plume itself, the signal-to-noise of the X-ray data is relatively low, making it difficult to set meaningful limits. Further observations of Abell 1914 with higher resolution X-ray telescopes, such as *Chandra* may prove more revealing.

In conclusion, we find that the amount of clearly identified tidal debris at our observational limits varies significantly from cluster to cluster. However, some clusters have strong tidal activity that ranges over physical scales of hundreds of kiloparsecs, and in at least one case, follows an asymmetric dark matter distribution, perhaps due to the stripping of dark matter from galaxy halos.

## 7. COMPARING TO SIMULATIONS

To place our observational study of the ICL in a more dynamical context, we compare our deep imaging to simulations of cluster collapse in a cosmological setting. Most previous simulations of tidal stripping and ICL formation have been based on simulations of individual galaxies moving through an established cluster potential (e.g., Richstone & Malumuth 1983; Miller 1983; Merritt 1983, 1984). However, the dynamics of cluster formation and tidal stripping are much more complex – clusters grow hierarchically, with small groups of galaxies accreted as the cluster grows larger and larger. Within these small groups, the tidal interactions can be slower and more dramatic, liberating a substantial amount of intracluster starlight (e.g., Mihos 2003). More recent simulations have studied the evolution of galaxies in a dynamically evolving cluster, giving a more realistic view of the forming ICL.

To visualize the formation of diffuse light in galaxy clusters, we use N-body simulations of galaxy clusters from Dubinski et al. (2003). Full details of the simulation technique can be found in Dubinski (1998) and Dubinski et al. (2003); we summarize the salient points here. The simulations were created by first evolving a cosmological  $\Omega_M = 1$  dark matter simulation, identifying bound clusters ( $M \sim 10^{14} M_\odot$ ,  $\sigma_v$  300 – 600 km/s) at  $z = 0$ , and replacing the 300 most massive halos at  $z = 3$  destined to lie within the  $z = 0$  cluster with composite disk/bulge/halo galaxy models. Upon replacement, the galaxy models are scaled in mass and size such that they retain a constant surface density and follow the Tully-Fisher relationship (see Dubinski 1998 and Dubinski et al. 2003 for details). A total of 3,600,000 particles comprise the luminous portions of the galaxies; these particles were used to construct artificial images of the clusters. While the use of an  $\Omega_M = 1$  simulation may seem questionable in the light of modern  $\Lambda$  cosmologies, it should have only modest impact on our main results. In the evolution of rich clusters, cosmology contributes largely through the evolving accretion rate onto the cluster, so that these simulations will have proportionally larger late-time accretion than in  $\Lambda$  cosmologies. We comment further on this effect below.

We create artificial images of these simulations by first spatially binning the particles to a comparable physical scale as our CCD images – in this case, one pixel corresponds to 800 pc. We assign each pixel a luminosity based on a V-band mass-to-light ratio of 5, typical of an old stellar population. We then smooth the image using a locally varying smoothing kernel which depends on both the mass density within the pixels and the “filling factor” of neigh-

boring pixels. The intent of this smoothing is to reduce the graininess inherent in  $N$ -body simulations, but we run the risk of over-smoothing the data in regions of very low density, artificially creating diffuse extended features. To prevent this, we limit the smoothing kernel in low density regions to a maximum  $\sigma = 8$  kpc. After this step, we re-bin in  $11 \times 11$  pixels and calculate a robust mean surface brightness in an identical fashion to that done for the real observational data.

The simulated cluster images are shown in Figure 13, color coded by surface brightness in the same fashion as the real observed clusters in Figure 7. Each frame is approximately 2.3 Mpc on a side. The greyscale intensities show surface brightnesses below  $\mu_V = 28$ , where the structure of the images begins to become mottled by discreteness noise in the simulation. The faintest structures seen in these images have  $\mu_V \sim 30$ , well below our observational detection limit. The top four panels show the evolution of an individual cluster over time. We caution that these images are not meant to simulate the appearance of high redshift clusters – we do not include  $(1+z)^4$  dimming, K-corrections, or an evolving mass-to-light ratio for the stellar populations. Instead, we are simply looking at how dynamical evolution and tidal stripping build up the diffuse ICL, and redshift is used here only as a dynamical clock for the cluster. The bottom panels show four different simulated clusters at  $z = 0$ , illustrating the wide variety of morphological features shown by evolved clusters.

Comparing our observational data to the simulations, it is clear we are just glimpsing the tip of the iceberg in terms of the spatial structure of the ICL. At  $\mu_V \sim 26$ , the isophotes are fairly regular; slight asymmetries show up at  $\mu_V \sim 27$  – compare the irregular envelope of cluster C6 with similar features in the cD cluster Abell 1413 (Paper I). At  $\mu_V \sim 27$  we also see the kind of “common envelope” features seen in some of our real systems, most notably Abell 1553. At the limit of our current detections,  $\mu_V \sim 28$ , more asymmetries show up in the evolved clusters, such as the plumes to the lower right in C2 and C4. However, the most interesting dynamical features – large scale plumes and streams – show up at even lower surface brightnesses,  $\mu_V \sim 30$ . To probe these structures, much deeper imaging is needed; here, issues of flat fielding, scattered light, and sky variability will become severe.

Figure 13 also shows how the morphology of the ICL changes with dynamical time. Early in the cluster’s history, as the bulk of the cluster is being assembled, significant tidal stripping results in plumes and arcs at relatively high surface brightness,  $\mu_V < 26$ . These features can be quite thin and sharp, and such features are likely a sign of a major, recent stripping event in the cluster. The relatively high surface brightness arcs seen in several nearby clusters (Trentham & Mobasher 1998; Gregg & West 1998; Calcaneo-Roldan et al. 2000) are likely examples of recent stripping. As the cluster evolves, many of these features “mix away,” creating a smoother ICL at these surface brightnesses in the more evolved clusters. In this context it is again interesting to note that we see more substructure in our non-cD clusters presented here than in the cD clusters of Paper I. Inasmuch as the presence of a cD galaxy indicates an evolved cluster, this difference in

ICL properties between cD and non-cD clusters is as expected from these evolutionary models.

We can quantify these isophotal asymmetries in a similar fashion to that done for the observational data – through a measurement of the centroid shift as a function of surface brightness. As with the observational data, we mask regions well outside the main body of the cluster and then calculate the isophotal centroids. In the 9 simulated clusters, we found spatial offsets between the  $\mu_V = 24$  and  $\mu_V = 26$  isophote which ranged from 0–35 kpc, and from 10–65 kpc for the offset between  $\mu_V = 24$  and  $\mu_V = 28$ . The cluster-to-cluster variation is large, with some very smooth clusters (like cluster C4 in Figure 13) showing little or no offset at all. These spatial offsets are similar to those seen in our Abell clusters – the large offsets are comparable to those observed in Abell 1234 and Abell 1914, while several of our clusters show no significant offsets at all.

Finally, we can look at the fraction of material in the simulated images as a function of limiting surface brightness. This measurement is perhaps the most uncertain, since it depends both on the adopted M/L value for the stars *and* the assumption that this value is fixed across the cluster. Nonetheless, we can get a simple estimate of the amount of material in the ICL for comparison to our observationally-derived numbers in Table 5. Figure 14 shows the fractional ICL as a function of limiting surface brightness for the nine evolved cluster simulations of Dubinski et al. (2003). At high surface brightness,  $\mu_V \sim 26$ , 8–18% of the cluster luminosity is in the diffuse component; this number drops to  $\sim 3$ –6% at  $\mu_V = 28$ . At low surface brightness, our observed ICL fraction is lower than the simulations, likely because we are simply nearing our detection limit. At higher surface brightness, we actually detect more ICL than simulated – a number of effects could be causing this. First, background contamination in the observational data would increase the amount of flux at low surface brightness. Secondly, and more importantly, the simulation data employs only luminous disk galaxies. A population of low surface brightness dwarf galaxies, or even the extended low surface brightness envelopes of elliptical galaxies, would raise the diffuse light content of the simulated galaxies significantly. Figure 14 shows the evolution of the amount of diffuse light in the evolving cluster. Early in the cluster’s history, as the bulk of the cluster is assembled, the diffuse light content increases quickly. At later times the ICL fraction oscillates, due largely to the accretion of infalling groups. As groups fall in to the cluster environment, they first reduce the fractional ICL by raising the high surface brightness content of the cluster. As they then orbit through the cluster and are tidally stripped, the diffuse light content of the cluster rises again. The magnitude of these fluctuations may well be a feature of the  $\Omega_M = 1$  cosmology, with its significant late accretion – clusters in a low  $\Omega_M$  universe may show this effect at a much lower level.

Any more quantitative analysis needs more sophisticated models employing a modern  $\Lambda$  cosmology and mix of progenitor types – models which are currently being developed (e.g., Napolitano et al. 2003; Dubinski et al. 2003; Mihos et al., in preparation). Nonetheless, even the simulated images presented here reveal striking sim-

ilarities with the observational data – to the depths that we currently probe, the detected morphology shows many of the structural features (common envelopes, faint arcs and plumes, and isophotal centroid shifts) evidenced in the dynamical models. However, these simulations also point toward the wealth of information contained in the detailed morphology and kinematics of the ICL lying just out of reach of current observational data. Deeper imaging, along with followup spectroscopy of PNe in nearby clusters to determine the kinematics of diffuse light, is a promising avenue toward unraveling the structure of the ICL.

## 8. SUMMARY

We have surveyed four Abell type II-III (non-cD) galaxy clusters, and find a significant amount of intracluster light in all of them. The amount of intracluster starlight is intermediate, approximately 10–20% of the galaxy light. This may reflect the dynamical adolescence of these galaxy clusters: as the clusters continue to evolve the mean intracluster fraction should increase. However, it is likely that cluster mass (or richness) also plays a role: both our own measurements of the rich cluster Abell 1413 (Paper I), and other studies of richer clusters such as Coma (Bernstein et al. 1995) find significantly higher intracluster star fractions than the clusters studied in this paper. Clearly, more observations of clusters over a range of cluster richnesses will be important to separate the two related effects.

We have searched for signs of asymmetries and tidal debris in the intracluster light, and we find multiple examples of these features, though in some clusters we found signs of a regular symmetric structure in the intracluster light and few tidal features. The number of tidal features in Abell 1914 is clearly unusual, in both number and surface brightness. It is worth reiterating here that Abell 1914 has a radio halo (Giovannini, Tordi, & Feretti 1999; Kempner & Sarazin 2001) and is believed to be undergoing a cluster merger (Jones et al. 2001). Therefore, the wealth of high surface brightness tidal features in the ICL in Abell 1914 is likely to be due to the ongoing cluster merger. We may be observing the cluster in *flagrante delicto*: had we observed the cluster a few crossing times later, the evidence of such a strong merger would be much less apparent.

Comparing our observational results to modern numerical simulations of galaxy clusters, we find good overall qualitative agreement in both the amount and distribution of the intracluster light, although the simulations show that significant ICL substructure may exist well below current detection levels. From the results found here, we suggest that intracluster light may act as a dynamical “clock” of galaxy clusters, one that is complementary to other studies of galaxy clusters such as X-ray substructure, weak lensing, and galaxy radial velocities. However, the comparison of ICL properties and models of structure formation and evolution is still in its infancy. A detailed comparison of the two will require much deeper ICL imaging and measurements of the kinematics of the ICL (though planetary nebulae velocities, for example), as well as through numerical simulations that have larger dynamical range, and better descriptions of galaxy formation processes. Such studies are now underway.

We thank the KPNO staff for their assistance with the observations. We especially thank William Baum for his communication regarding the early study of Abell 801. We also thank Cameron McBride for a large, yet oddly undefinable, range of technical and scientific support. This work is supported by NSF through grants AST-9876143 (JCM), AST-9624542 (HLM), and AST-0302030 (JF). Funding was also given by the Research Corporation’s Cottrell Scholarships (JCM and HLM). We also thank an anonymous referee for suggestions that improved the presentation of this data. This research has made use of the USNOFS Image and Catalogue Archive operated by the United States Naval Observatory, Flagstaff Station (<http://www.nofs.navy.mil/data/fchpix/>). This research has made use of data obtained through the High Energy Astrophysics Science Archive Research Center Online Service, provided by the NASA/Goddard Space Flight Center.

## APPENDIX

## THE ERROR MODEL

It is necessary to have accurate error estimates of our surface photometry in order to perform the model fitting. Unlike earlier photographic work, deep CCD surface photometry allows us to quantify measurement errors. Measurement errors arise from CCD behaviors such as readout noise and flat-fielding, as well from sky noise. Each error contribution will be addressed below.

## READOUT NOISE

The readout noise per exposure is 1.1 ADU. By combining  $N_G$  images with a median, we are able to reduce the effective read noise to

$$R_{eff} = 1.1 \text{ ADU} \frac{1.22}{\sqrt{N_G}} \quad (\text{B1})$$

The factor of 1.22 is due to the lower efficiency of a median over a mean (see Morrison, Boroson, & Harding 1994, Section 3.2.1).

## PHOTON NOISE

For  $C$  ADU in a given pixel, the photon noise is  $(C/g)^{1/2}$ , where  $g$  is the gain. Combining  $N_G$  images respectively using a median reduces the photon noise to

$$\sigma_{Poisson} = \frac{1.22}{\sqrt{N_G}} \frac{\sqrt{C}}{\sqrt{g}} \quad (\text{C1})$$

## LINEARITY ERRORS

As mentioned in §5.2 above, the T2KA chip has a known non-linearity. We have corrected for this effect, but the parameters used for the correction do not have infinite precision, and so our correction has errors. The error in flux can be derived as follows:

$$\sigma_{linearity}^2 = \sigma_{c1}^2 C_{sky}^2 + \sigma_{c2}^2 \frac{C_{sky}^4}{(32767)^2} + \sigma_{c3}^2 \frac{C_{sky}^6}{(32767)^4} \quad (\text{D1})$$

where  $C_{sky}$  is the sky-subtracted flux. Since this correction is small, we apply it only to the flux, and not to any other calibration image.

## FLAT-FIELDING ERRORS

In principle, the only limit to the precision of the combined flat-field images is the photon noise in the individual flat-field images. This small-scale variation is

$$\sigma_{sff} = \frac{\sqrt{C_s}}{\sqrt{g}} \frac{1.22}{\sqrt{N_f}} \frac{1.22}{\sqrt{N_G}} \quad (\text{E1})$$

where  $C_s$  is the number of counts in the final, combined master sky flat image,  $g$  is the gain,  $N_f$  is the number of individual sky flats used to make the master sky flat, and  $N_G$  is the number of individual galaxy images used to make the final galaxy image.

In practice, the small-scale flat-fielding errors are not the only flat-fielding error we have. There are also large-scale variations which arise from the variation of the sky brightness across the image, instrumental effects such as flexure, and from the wings of bright stars and galaxies that were not completely removed by combining the individual sky flats. Normally, to measure this effect, we prefer to divide our sky flats into two sub-samples, create two sky flat images from those sub-samples, and then find the standard deviation of the ratio of the two created flats. However, we have few sky images, and dividing them up into two ten image sub-samples would be too noisy for a realistic measurement.

Instead, we masked each image, and constructed a histogram of sky values (§5.2), and determined the large-scale flat-fielding error from those histograms. Generally, this large-scale flat-fielding error is the dominant source of error at low surface brightnesses.

## SURFACE BRIGHTNESS FLUCTUATIONS

For ultra-deep surface brightness observations of nearby galaxies, a major source of error arises from intrinsic surface brightness variations (Tonry & Schneider 1988). For our distant galaxy clusters (see eq 10 of Tonry & Schneider (1988)), such an effect is completely negligible compared to our other errors.

## REFERENCES

- Abell, G. O. 1962, in *Problems of Extragalactic Research*, ed. McVittie, G. C. (New York: The Macmillan Company)
- Abell, G. O., Corwin, H. G., & Olowin, R. P. 1989, *ApJS*, 70, 1
- Adams, F. & Laughlin, G. 1999, *The five ages of the Universe: Inside the physics of eternity* (The Free Press: New York)
- Arnaboldi, M., Freeman, K. C., Méndez, R. H., Capaccioli, M., Ciardullo, R., Ford, H., Gerhard, O., Hui, X., Jacoby, G. H., Kudritzki, R. P., & Quinn, P. J., 1996, *ApJ*, 472, 145
- Baum, W. A. 1973, *PASP*, 85, 530
- Bautz, L. P. & Morgan, W. W. 1970, *ApJ*, 162, L149
- Beckers, J. 1995, in *Scientific and Engineering Frontiers for 8-10m Telescopes*, ed. M. Iye and T. Nishimura (Tokyo, Universal Academy), p. 303
- Bernstein, G. M., Nichol, R. C., Tyson, J. A., Ulmer, M. P., & Wittman, D. 1995, *AJ*, 110, 1507
- Bertin, E. & Arnouts, S. 1996, *A&AS*, 117, 393
- Böhringer, H. et al. 2000, *ApJS*, 129, 435
- Böhringer, H., Briel, U. G., Schwarz, R. A., Voges, W., Hartner, G., & Trumper, J. 1994, *Nature*, 368, 828
- Bothun, G., Impey, C., & McGaugh, S. 1997, *PASP*, 109, 745
- Bucknell, M. J., Godwin, J. G., & Peach, J. V. 1979, *MNRAS*, 188, 579
- Buote, D. A. 2002, *ASSL Vol. 272: Merging Processes in Galaxy Clusters*, 79
- Buote, D. A. 2001, *ApJ*, 553, L15
- Buote, D. A. & Tsai, J. C. 1996, *ApJ*, 458, 27
- Burns, J. O., Rhee, G., Owen, F. N., & Pinkney, J. 1994, *ApJ*, 423, 94
- Busko, I. C. 1996, *ASP Conf. Ser. 101: Astronomical Data Analysis Software and Systems V*, 5, 139
- Calcáneo-Roldán, C., Moore, B., Bland-Hawthorn, J., Malin, D., & Sadler, E. M. 2000, *MNRAS*, 314, 324
- Capaccioli, M., Held, E. V., Lorenz, H., & Vietri, M. 1990, *AJ*, 99, 1813
- Coleman, G. D., Wu, C.-C., & Weedman, D. W. 1980, *ApJS*, 43, 393
- Dahle, H., Kaiser, N., Irgens, R. J., Lilje, P. B., & Maddox, S. J. 2002, *ApJS*, 139, 313
- David, L. P., Forman, W., & Jones, C. 1999, *ApJ*, 519, 533
- de Vaucouleurs, G. 1948, *Ann. Astrophys*, 11, 247
- De Vaucouleurs, G., De Vaucouleurs, A., Corwin Jr., H.G., Buta, R. J., Paturel, G., & Fouque, P. 1991, *Third Reference Catalogue Of Bright Galaxies*, Version 3.9
- Dressler, A. 1984, *ARA&A*, 22, 185
- Drinkwater, M. J., Gregg, M. D., Hilker, M., Bekki, K., Couch, W. J., Ferguson, H. C., Jones, J. B., & Philipps, S. 2003, *Nature*, 423, 519
- Dubinski, J. 1998, *ApJ*, 502, 141
- Dubinski, J., Koranyi, D., & Geller, M. 2003, *IAU Symposium*, 208, 237
- Durrell, P., Ciardullo, R., Feldmeier, J. J., Jacoby, G. H., & Sigurdsson, S. 2002, *ApJ*, 570, 119
- Feldmeier, J. J., Mihos, J. C., Morrison, H. L., Rodney, S. A., & Harding, P. 2002 (Paper I), *ApJ*, 575, 779
- Feldmeier, J. J., Ciardullo, R., & Jacoby, G. H. 1998, *ApJ*, 503, 109
- Feldmeier, J. J., Ciardullo, R., & Jacoby, G. H., & Durrell, P. 2004, *ApJ*, in press
- Ferguson, H. C., Tanvir, N. R., & von Hippel, T. 1998, *Nature*, 391, 461
- Feretti, L. 1999, in *Proc. of the Workshop Diffuse Thermal and Relativistic Plasma in Galaxy Clusters*, ed. H. Böhringer, L. Feretti, P. Schuecker, & V. K. Kapahi (MPE Rep. 271; Garching: Max Planck Institut für Extraterrestrische Physik), 1
- Fry, A. M., Morrison, H. L., Harding, P., Boroson, T. A., 1999, *AJ*, 118, 1209
- Giovannini, G., Tordi, M., & Feretti, L. 1999, *New Astronomy*, 4, 141
- Girardi, M. & Biviano, A. 2002, *ASSL Vol. 272: Merging Processes in Galaxy Clusters*, 39
- Gnedin, O. Y. 2003, *ApJ*, 589, 752
- Gonzalez, A. H., Zabludoff, A. I., Zaritsky, D., & Dalcanton, J. J. 2000, *ApJ*, 536, 561
- Gregg, M. D., & West, M. J. 1998, *Nature*, 396, 549
- Grego, L., et al. 2001, *ApJ*, 552, 2
- Gudehus, D. H. 1989, *ApJ*, 340, 661
- Hibbard, J. E., Guhathakurta, P., van Gorkom, J. H., & Schweizer, F. 1994, *AJ*, 107, 67
- Ikebe, Y., Reiprich, T. H., Böhringer, H., Tanaka, Y., & Kitayama, T. 2002, *A&A*, 383, 773
- Jedrzejewski, R. I. 1987, *MNRAS*, 226, 747
- Jones, M. E., et al. , *MNRAS*, submitted - available as astro-ph 0103046
- Kempner, J. C. & Sarazin, C. L. 2001, *ApJ*, 548, 639
- Korchagin, V., Tsuchiya, T., & Miyama, S. M. 2001, *ApJ*, 549, 244.
- Krisциunas, K. 1997, *PASP*, 109, 1181
- Krisциunas, K. & Schaefer, B. E. 1991, *PASP*, 103, 1033
- Landolt, A. U. 1992, *AJ*, 104, 340.
- Ledlow, M. J. & Owen, F. N. 1995, *AJ*, 110, 1959
- Leir, A. A. & van den Bergh, S. 1977, *ApJS*, 34, 381
- Malin, D. F. & Carter, D. 1983, *ApJ*, 274, 534
- Merritt, D. 1983, *ApJ*, 264, 24
- Merritt, D. 1984, *ApJ*, 276, 26
- Merritt, D. 1985, *ApJ*, 289, 18
- Mihos, J. C. 2003, in *Carnegie Observatories Astrophysics Series, Vol. 3: Clusters of Galaxies: Probes of Cosmological Structure and Galaxy Evolution*, ed. J. S. Mulchaey, A. Dressler, and A. Oemler (Pasadena: Carnegie Observatories, <http://www.ociv.edu/ociv/symposia/series/symposium3/proceedings.html>)
- Miller, G. E. 1983, *ApJ*, 268, 495
- Mochejska, B. J., Kaluzny, J., Stanek, K. Z., Sasselov, D. D., & Szentgyorgyi, A. H. 2001, *AJ*, 121, 2032.
- Morrison, H. L., Boroson, T. A. & Harding P., 1994, *AJ*, 108, 1191
- Morrison, H. L., Miller, E. D., Harding, P., Stinebring, D. R., & Boroson, T. A. 1997, *AJ*, 113, 2061
- Moore, B., Katz, N., Lake, G., Dressler, A., & Oemler, A. 1996, *Nature*, 379, 613
- Napolitano, N. R. et al. 2003, *ApJ*, 594, 172
- Owen, F. N., White, R. A., & Ge, J. 1993, *ApJS*, 87, 135
- Quilis, V., Moore, B., & Bower, R. 2000, *Science*, 288, 1617
- Racine, R. 1996, *PASP*, 108, 699
- Richstone D. O., & Malumuth, E.M. 1983, *ApJ*, 268, 30
- Roach, F. E. & Grodon, J. L. 1973, *The Light of the Night Sky* (Dordrecht, Reidel)
- Schechter, P. 1976, *ApJ*, 203, 297
- Schombert, J.M. 1988, *ApJ*, 328, 475
- Shibata, R. et al. 2001, *ApJ*, 549, 228
- Soltan, A. & Henry, J. P. 1983, *ApJ*, 271, 442
- Stetson, P. B. 1987, *PASP*, 99, 191.
- Struble, M. F. & Rood, H. J. 1987, *ApJS*, 63, 555
- Struble, M. F. & Rood, H. J. 1999, *ApJS*, 125, 35
- Tonry, J. & Schneider, D. P. 1988, *AJ*, 96, 807
- Tonry, J. L., Ajhar, E. A., & Luppino, G. A. 1990, *AJ*, 100, 1416
- Trentham, N. & Mobasher, B. 1998, *MNRAS*, 293, 53
- Trentham, N. & Hodgkin, S. 2002, *MNRAS*, 333, 423
- Uson, J. M., Boughn, S. P., & Kuhn, J. R. 1991, *ApJ*, 369, 46
- Víchez-Gomez, R., Pelló, R. & Sanahuja, B. 1994, *A&A*, 283, 37
- White, D. A. 2000, *MNRAS*, 312, 663
- Wild, W. J. 1997, *PASP*, 109, 1269
- Willman, B., Governato, F., Mayer, L. & Quinn, T. 2004, *ApJ*, in prep
- Wilson, G., Smail, I., Ellis, R. S., & Couch, W. J. 1997, *MNRAS*, 284, 915
- Yamagata, T. & Maehara, H. 1986, *PASJ*, 38, 661
- Zheng, Z. et al. (1999), *AJ*, 117, 2757
- Zwicky, F. 1951, *PASP*, 63, 61
- Zwicky, F., Sargent, W. L. W., & Kowal, C. T. 1975, *AJ*, 80, 545

TABLE 1  
TARGET INFORMATION

Cluster	RA <sup>a</sup>	Dec <sup>a</sup>	Richness <sup>a</sup>	Redshift <sup>b</sup>	Bautz-Morgan type <sup>c</sup>	Rood-Sastry type <sup>d</sup>
Abell 801	09h 28m 01.4s	+20d 33m 54s	2 (C = 81)	0.1918	II-III	B (b)
Abell 1234	11h 22m 26.2s	+21d 23m 32s	2 (C = 88)	0.1663	III	L (6)
Abell 1553	12h 30m 50.1s	+10d 34m 26s	2 (C = 100)	0.1652	III	L (4)
Abell 1914	14h 26m 03.0s	+37d 49m 32s	2 (C = 105)	0.1712	II:	L (6)

<sup>a</sup>Coordinates are cluster centers, C is the background-corrected count of cluster members between  $m_3$  and  $m_3 + 2$ , data taken from Abell, Corwin, & Olowin (1989).

<sup>b</sup>Data taken from Struble & Rood (1999)

<sup>c</sup>Data taken from Leir & van den Bergh (1977)

<sup>d</sup>Data taken from Struble & Rood (1987)

TABLE 2  
OBSERVING LOG & ADOPTED TARGET INFORMATION

Target	$N_{\text{exposures}}$	Median sky ( $\mu_V$ )	Median seeing (arcseconds)	Average HA (minutes)	Image size <sup>b</sup> (arcminutes)	Angular size <sup>c</sup> Distance (Mpc)	Image size (Mpc)	DM <sup>d</sup> (mag)
Abell 801	6	21.2	2.6	$-38 \pm 29$	$10.3 \times 9.9$	614.6	$1.8 \times 1.8$	39.7
Abell 1234	14	21.3	1.1	$-80 \pm 80$	$8.2 \times 9.2$	548.0	$1.3 \times 1.5$	39.4
Abell 1553	20	21.1	2.0	$16 \pm 70$	$9.8 \times 10.1$	545.0	$1.6 \times 1.6$	39.3
Abell 1914	11	21.6	1.0	$07 \pm 70$	$10.0 \times 9.9$	561.6	$1.6 \times 1.6$	39.4
Blank Sky	49	21.3	–	$-28 \pm 96$	–	–	–	–

<sup>a</sup>The error bars show the spread in the hour angle distribution for the source's exposures, not the error in the hour angle (which is negligible).

<sup>b</sup>Image dimensions are E-W by N-S, and show the final trimmed sizes of the images.

<sup>c</sup>Assuming our adopted cosmology ( $H_0 = 75$  km/s/Mpc,  $\Omega_m = 0.3$ ,  $\Omega_\Lambda = 0.7$ )

<sup>d</sup>Distance Modulus, assuming our adopted cosmology

TABLE 3  
ADOPTED LARGE-SCALE FLAT-FIELD ERRORS AND OBSERVATIONAL LIMITS

Target	Adopted error (ADU)	Notes	Percent Error	Total Bin error	$\mu_{1\sigma}$	$\mu_{5\sigma}$
Abell 801	0.6	standard deviation	0.07	0.91	28.58	26.83
Abell 1234	0.6	standard deviation	0.08	0.62	29.00	27.25
Abell 1553	1.5	visual inspection	0.17	1.53	28.01	26.26
Abell 1914	2.0	visual inspection	0.35	2.02	27.71	25.96

TABLE 4  
COMPARISON OF SURFACE PHOTOMETRY FOR 1119+216

Parameter	Ledlow & Owen (1995)	Our results
$r_{24.5}^a$	27.99 kpc	$29.0 \pm 1.6$ kpc
ellipticity ( $r_{24.5}$ )	0.298	$0.281 \pm 0.029$
PA ( $r_{24.5}$ )	$85^\circ$	$79.7^\circ \pm 3.2^\circ$

<sup>a</sup>Radius given is (ab)<sup>1/2</sup>

TABLE 5  
ISOPHOTAL ICL FRACTIONS

Target	$\mu_{limit} = 26.0$	$\mu_{limit} = 26.5$	$\mu_{limit} = 27.0$	$\mu_{limit} = 27.5$
Abell 801	$16 \pm 4.7\%$	$6.9 \pm 4.2\%$	$2.7 \pm 4.0\%^a$	$1.2 \pm 3.9\%^a$
Abell 1234	$17 \pm 4.4\%$	$10 \pm 4.1\%$	$4.9 \pm 3.9\%$	$2.1 \pm 3.7\%^a$
Abell 1553	$21 \pm 16\%$	$12 \pm 15\%^a$	$5.3 \pm 14\%^a$	$2.2 \pm 13\%^a$
Abell 1914	$28 \pm 16\%$	$15 \pm 14\%^a$	$6.8 \pm 13\%^a$	$2.9 \pm 13\%^a$
NGC 3379	7.8%	5.0%	3.9%	2.0%
NGC 3379 (trunc)	2.6%	0%	0%	0%

<sup>a</sup>This measurement is below  $\mu_{5\sigma}$  for this cluster

TABLE 6  
ICL LUMINOSITY AND LUMINOSITY DENSITIES

Target	$\mu_{limit} = 26.0$	$\mu_{limit} = 26.5$	$\mu_{limit} = 27.0$	$\mu_{limit} = 27.5$
Luminosity ( $10^{11}L_{\odot}$ ): <sup>a</sup>				
Abell 801	$1 \pm 0.3$	$0.8 \pm 0.5$	$0.4 \pm 0.6$	$0.3 \pm 1.0$
Abell 1234	$3 \pm 0.8$	$2 \pm 0.8$	$1 \pm 0.8$	$0.8 \pm 1.4$
Abell 1553	$3 \pm 2$	$2 \pm 3$	$1 \pm 3$	$0.7 \pm 4$
Abell 1914	$8 \pm 5$	$6 \pm 5$	$4 \pm 8$	$3 \pm 13$
Luminosity Density ( $10^5L_{\odot}\text{kpc}^{-2}$ ): <sup>a</sup>				
Abell 801	$10 \pm 3$	$6 \pm 4$	$4 \pm 6$	$3 \pm 10$
Abell 1234	$8 \pm 2$	$6 \pm 2$	$4 \pm 3$	$3 \pm 5$
Abell 1553	$8 \pm 6$	$5 \pm 6$	$4 \pm 10$	$2 \pm 12$
Abell 1914	$13 \pm 8$	$10 \pm 9$	$7 \pm 13$	$5 \pm 22$

<sup>a</sup>Assuming the adopted DM, but with no K-corrections. For  $V$  magnitudes, the K-corrections are on order of 0.4 magnitudes at these redshifts (Coleman, Wu, & Weedman 1980)



FIG. 1.— Our final, median-combined images for all of the observed clusters. The top left cluster is Abell 801, top right is Abell 1234, bottom left is Abell 1553, and the bottom right is Abell 1914. North is at the left of each image, and east is at the bottom. The image sizes are given in Table 2.

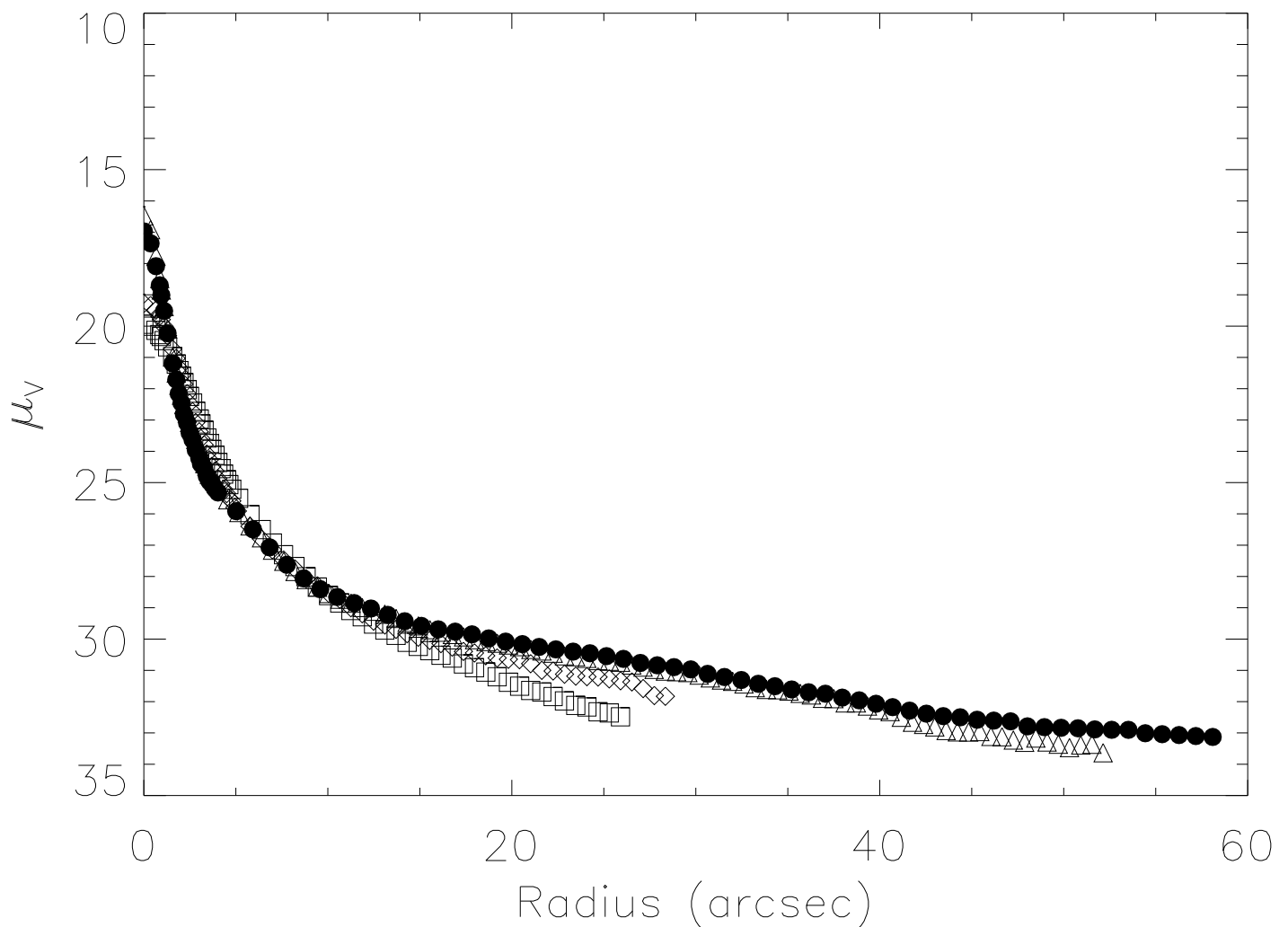


FIG. 2.— The surface brightness profile of a saturated star on each of our cluster images, averaged azimuthally (see the text on how these profiles were constructed). For comparison purposes, a constant has been added to each profile to make them equivalent at  $R=10$  arcseconds. The filled circles denote the surface brightness profile from Abell 1234, the open diamonds Abell 1553, the open triangles from Abell 1914, and the open squares are the profile from Abell 801. At small radii, the profiles vary significantly due to seeing, but there is excellent agreement at intermediate radii. Since each saturated star has a different apparent magnitude, the radius at where the profile diverges and blends into the background noise varies.

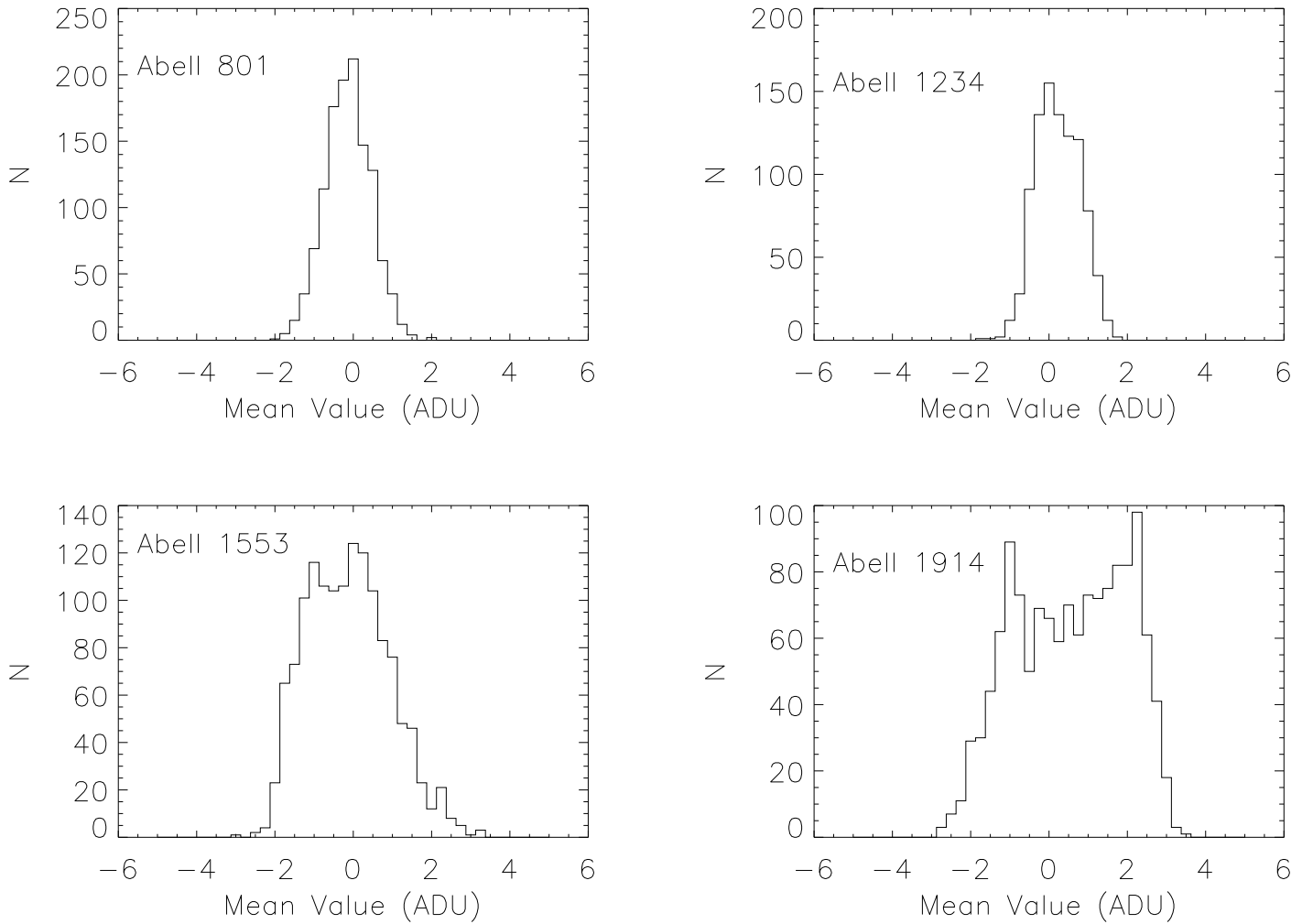


FIG. 3.— The histogram of sky values for each cluster, binned up into 0.25 ADU intervals. See the text for the description of how this histogram was created. Ideally, the sky values should all equal zero, but due to large-scale flat-fielding errors, and the faint unmasked wings of stars and galaxies, there is usually a dispersion about zero in observed data. Abell 801 and Abell 1234 have well-behaved sky histograms, with a well-defined mode, and whose probability distributions are approximately Gaussian (see Paper I, and Fry et al. (1999) for other such histograms), but Abell 1553 and Abell 1914 have broader sky histograms and are multi-modal due to large-scale flat fielding errors. See the text for further discussion.

FIG. 4.— A plot of sky values in Abell 1553 (top), and Abell 1914(bottom), plotted as a function of row number. The row number is equivalent to the E-W distance for the T2KA orientation. A clear systematic error is seen in both clusters.

FIG. 5.— The core of Abell 1234, multiplied by the isophotal mask. From left to right, and top to bottom, the surface brightness limit  $\mu_{limit}$  is 26, 26.5, 27, and 27.5, respectively. Note that the brighter surface brightness limits allow some galaxy light to “leak” around the edges of the mask. See the text for further discussion.

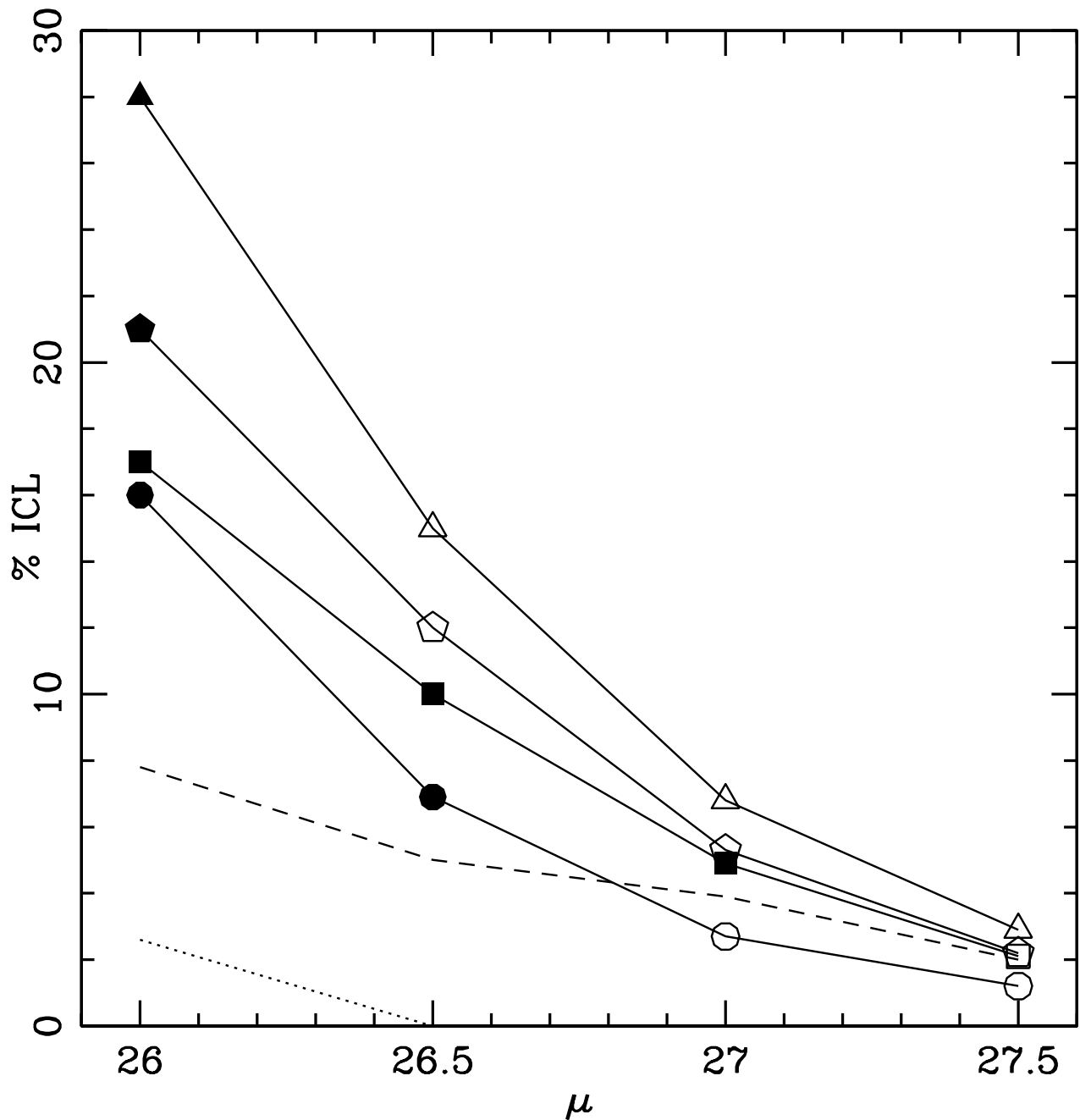


FIG. 6.— A comparison of the derived intracluster luminosity fractions for each cluster. Circles denote data from Abell 801, squares are from Abell 1234, pentagons are from Abell 1553, and the triangles denote data from Abell 1914. Filled points denote measurements above  $\mu_{5\sigma}$ , and open points denote measurements below  $\mu_{5\sigma}$ . These measurements are compared to models of the galaxy NGC 3379 (the dashed line), and NGC 3379 tidally truncated (the dotted line). See the text for further discussion. Note that the error bars have been omitted from this figure for clarity, but the errors are significant, varying from  $\approx 4\%$  for Abell 801 and 1234, and up to  $\approx 16\%$  for Abell 1553 and Abell 1914. The error bars are given explicitly in Table 5.

FIG. 7.— Images of Abell 801 (top left), and Abell 1234 (top right), Abell 1553 (bottom left), and Abell 1914 (bottom right binned up into  $11 \times 11$  pixels bins. North is left, and east is at the bottom of these images. The color black represents all bins with an average surface brightness from  $\mu_V = 20$  to 24, the color red represents all bins from  $\mu_V = 24$  to 26, the color green represents all bins from  $\mu_V = 26$  to 27 and the color blue represents all bins from  $\mu_V = 27$  to 28, which is only reliably reached in the Abell 801 and Abell 1234. All bins with surface brightnesses below  $\mu_V = 28$  (for Abell 801 and Abell 1234) or  $\mu_V = 27$  (for Abell 1553 and Abell 1914) are left uncolored. For Abell 801, a flat-fielding fluctuation can be seen at the top of the image, while for Abell 1553, and Abell 1914 the systematic large scale flat fielding error described in Figure 4 can be seen across the images. In Abell 1553, the bright compact galaxy pair VIII ZW 192 is present in the bottom right hand portion of the image (Zwicky, Sargent, & Kowal 1975).

FIG. 8.— Images of the central regions of each cluster, binned up into regions of  $11 \times 11$  pixels ( $3.3''$ ). From left to right and top to bottom they are Abell 801, Abell 1234, Abell 1553, and Abell 1914. North is to the left on each image, and east is at the bottom. The centroid is marked with the corresponding surface brightness limit. Abell 801 and 1553 have small deviations in the centroid position, where Abell 1234, and Abell 1914 have large deviations. See the text for further discussion.

FIG. 9.— Two images of a central portion of Abell 1553. The images are both  $96''$  square (corresponding to  $\approx 250$  kpc at our adopted distance). North is to the left, and east is at the bottom of these images. The greyscale of both images runs from  $\mu_V = 24.6$  (black) to  $\mu_V = 29$  (white). On the left is the reduced image, without any masking or binning. A plume-like surface brightness feature is clearly visible extending from the most luminous galaxy towards the southeast. The surface brightness of this feature is approximately  $\mu_V = 25.1$ . On the right is the same image, but binned up into  $11 \times 11$  pixels, and with the smaller galaxies masked. In this figure, the brighter plume is connected with a much fainter plume of average surface brightness of  $\mu_V = 26.3$ . The small white points denote the approximate extent of this fainter plume. See the text for further discussion.

FIG. 10.— A  $4.0'$  by  $3.1'$  image of the central region of Abell 1914. North is to the left and east is at the bottom of this figure. The five tidal features discussed in the text are labeled.

FIG. 11.— A  $2.0'$  by  $1.6'$  image of the western arc of Abell 1914. North is to the left, and east is at the bottom of this figure. The dark lines outline the arc structure, which is approximately  $1'$  long, and  $12''$  wide at the widest point. Note the diffuse structure of the arc, unlike those found from gravitational lensing.

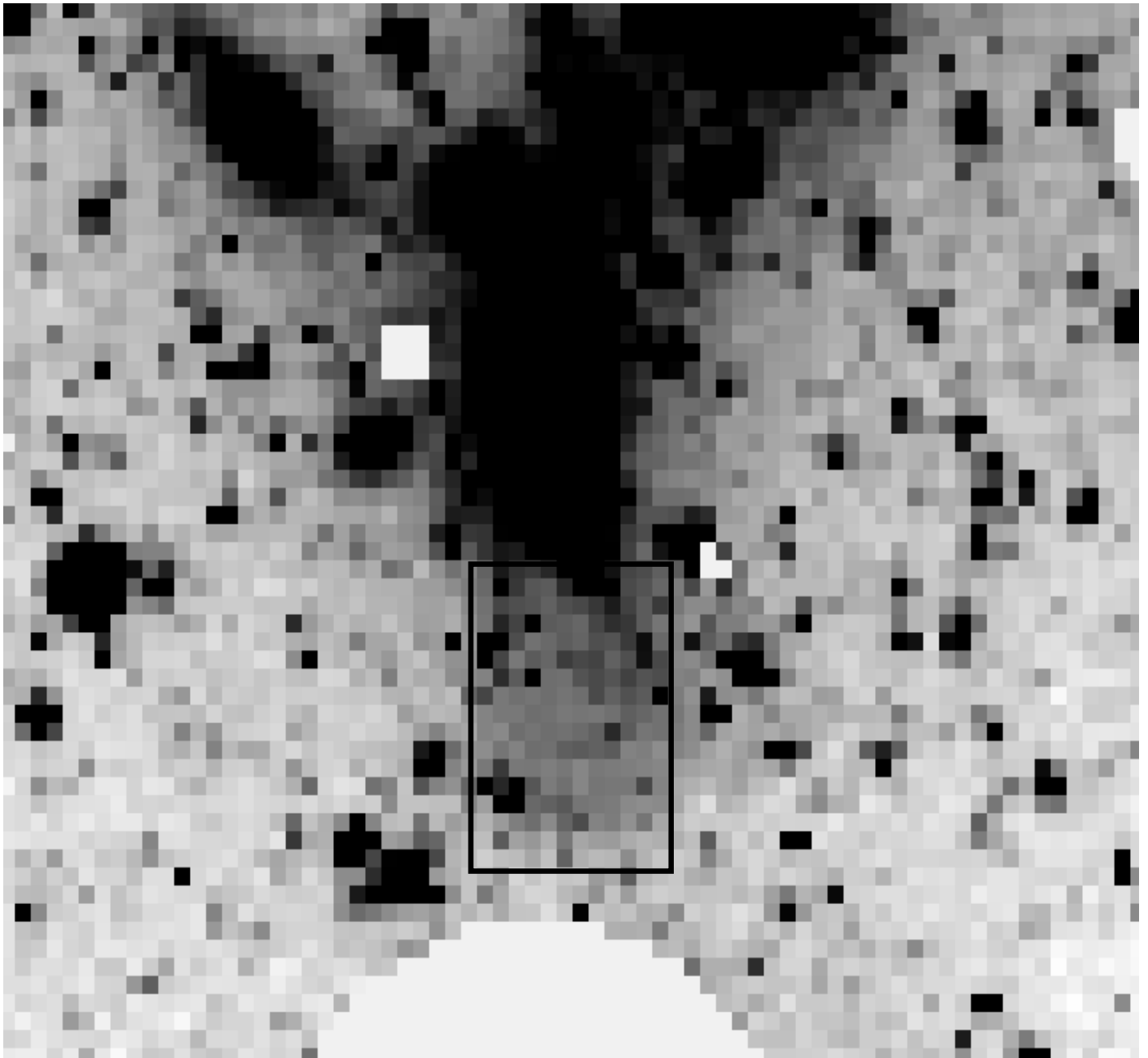


FIG. 12.— A  $4.0'$  by  $3.2'$  image of the eastern plume of Abell 1914. North is to the left, and east is at the bottom of this figure. The dark lines outline the structure of the plume, which is extremely elongated, and has a steep surface brightness gradient. The large white circle at the bottom of this image is the edge of a saturated star.

FIG. 13.— Images of some of the simulated clusters of Dubinski (1998), colored in an identical way as in Figure 7. The top row shows a single cluster as it evolves over time, while the bottom column shows four clusters of different morphologies at  $z = 0$ . Note the asymmetric surface brightness distribution at lower surface brightnesses, and the range of ICL properties. See the text for further discussion.

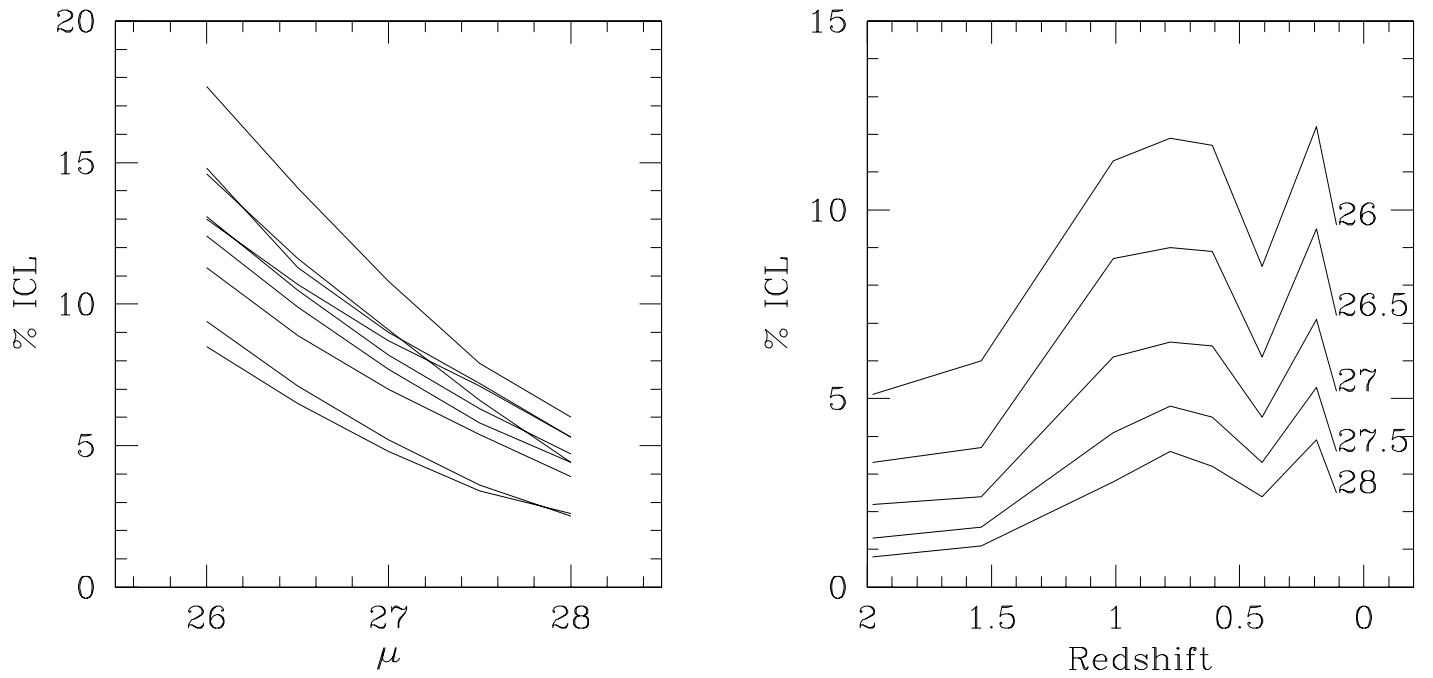


FIG. 14.— The ICL luminosity fraction found in the simulations by Dubinski et al. (2003), as a function of surface brightness, measured in an identical way as the observations. On the left is the results from nine clusters determined at a redshift of zero. On the right is the results from a single evolving cluster as a function of redshift. See the text for further explanation.

This figure "f1.jpg" is available in "jpg" format from:

<http://arxiv.org/ps/astro-ph/0403414v1>

This figure "f5.jpg" is available in "jpg" format from:

<http://arxiv.org/ps/astro-ph/0403414v1>



This figure "f7.jpg" is available in "jpg" format from:

<http://arxiv.org/ps/astro-ph/0403414v1>

This figure "f8.jpg" is available in "jpg" format from:

<http://arxiv.org/ps/astro-ph/0403414v1>

This figure "f9a.jpg" is available in "jpg" format from:

<http://arxiv.org/ps/astro-ph/0403414v1>

This figure "f9b.jpg" is available in "jpg" format from:

<http://arxiv.org/ps/astro-ph/0403414v1>

This figure "f10.jpg" is available in "jpg" format from:

<http://arxiv.org/ps/astro-ph/0403414v1>

This figure "f11.jpg" is available in "jpg" format from:

<http://arxiv.org/ps/astro-ph/0403414v1>

This figure "f13.jpg" is available in "jpg" format from:

<http://arxiv.org/ps/astro-ph/0403414v1>